2012

GENERATION, MECHANICAL AND STATISTICAL ANALYSIS, AND FEM SIMULATION OF FRACTURE OF REPEATABLE RANDOM ROUGH SURFACES

Hector Medina
Virginia Commonwealth University

GENERATION, MECHANICAL AND STATISTICAL ANALYSIS, AND FEM SIMULATION OF FRACTURE OF REPEATABLE RANDOM ROUGH SURFACES

A Thesis submitted in partial fulfillment of the requirements for the degree of Master of Science at Virginia Commonwealth University.

By

HECTOR EDUARDO MEDINA
B.S. in Engineering, Mechanical Specialty, Colorado School of Mines, USA, 1994

Director: BRIAN HINDERLITER
ASSOCIATE PROFESSOR, DEPARTMENT OF MECHANICAL AND NUCLEAR ENGINEERING

Virginia Commonwealth University
Richmond, Virginia
May 2012

Acknowledgement

At submitting this document, I would like to acknowledge the patient help of two persons: Dr. Brian Hinderliter and Dr. Karla Mossi.

Dr. Brian Hinderliter has been more than an adviser but a mentor and a friend who has gained my trust as a professional and an individual with virtues that made my research experience rather pleasant. His manifold understanding and vigorous academic observation enlightened my research on its different aspects.

As for Dr. Mossi, her patience and care, professionalism and hard work as the Department of Mechanical's Graduate Program director are evident. I always wondered how she could manage to assist all of us, and be successful at her own research, as well.

A thousand thanks, to my daughters Nazareth and Hecdalis for understanding my undertaking.

"*He has brought me here, will continue to guide me and eventually take me Home, by Faith*".

Table of Contents

Page

List of Tables

Page

List of Figures

Page

Abstract

Generation, Mechanical and Statistical Analysis, and FEM Simulation of Fracture of Repeatable Random Rough Surfaces

By Hector Medina, *MS*

A Thesis submitted in partial fulfillment of the requirements for the degree of Master in Science at Virginia Commonwealth University.

Virginia Commonwealth University, 2012

Major Director: Dr. Brian Hinderliter, Ph.D.
Associate Professor, Mechanical and Nuclear Engineering

Natural weathering and wear of structural materials in service nearly always generate surface roughness, and follow the Central Limit Theorem prediction for surface topology. This study couples experimental and statistical theory, and FEM to extend knowledge of life of materials from initial service surface conditions through surface damage accumulation. Statistical moments and other parameters were correlated with fracture locations probability ($\mathcal{H}/\mathcal{N}$), versus auto correlation length, and depth. As the surface grows to a full Gaussian, $\mathcal{H}/\mathcal{N}$ increases its dependence on profile's Average and RMS Roughness, and derived parameters. This dependence shows an asymptotic limit behavior that approaches agreeably Griffith's crack criterion, though with multiple pit

locations. Importantly, a Transitional Region was observed, below which the probable location of fracture is uncorrelated to the parameters studied. This is because introduced roughness is insufficient to compete with impurities, internal and external manufacturing flaws, and scratches, due to handling and machining, on the samples.

Chapter 1 Introduction

1.1 Economic Motivation

Despite the fact that catastrophic failure offers profits for attorneys and consulting engineers, such events are damaging to the economy as a whole. Undoubtedly, the economic cost of fracture and its prevention is quite large [1, 26]. Regardless of the considerable advancement on our understanding of material fracture, still structures are overdesigned as to assure reliability, thus increasing their cost [27]. A study by the Department of Commerce completed in past years showed that the annual cost of fracture (not including the effects of wear or corrosion) of materials in the United States represented about 4% of the Gross National Product (GNP), which infers a rather significant use of resources and manpower [26]. According to similar studies, if wear and corrosion effects were added to that noteworthy figure, costs would elevate to about 10% of the GNP [1]. Europe has reported comparable percentages [28]. Therefore, it is quite reasonable to assume that similar to higher values are likely to apply to all developed countries [1].

1.2 Basic Concepts

Roughness is one of the main factors influencing wear and crack initiation and propagation [29]. Under some proper loading, valleys of rough surfaces can be thought of as surface crack initiators [30]. By surface, it is meant the geometrical boundary between a solid and the environment. Now, Random Roughness (RR) has been defined as the standard error of

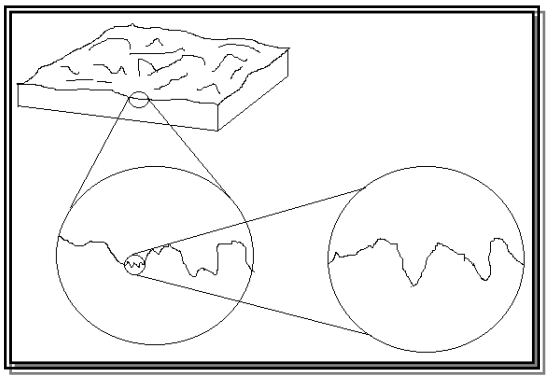

Fig. 1.1- Even seemingly flat areas of a surface are rough under some fine-scale spatial resolution

individual elevations after oriented roughness has been removed [2]. Or analogically stated, RR can be described as the standard deviation of elevation from a plane across a tilled surface, once oriented roughness is considered for. The influence of Random Roughness on surfaces is very important as it is a phenomenon that continuously takes place in nature and on engineering surfaces [21]. It can reasonably be stated that virtually, under some fine-scale spatial resolution, RR is present almost everywhere, figure 1.1 [36, 37]. For instance, textures of most engineering surfaces, which are a function of both its production process and the nature of the parent material, are random [3]. It is, therefore, of much interest to further understand the effects of random roughness on material failure as it models real situations.

1.3 Some Applications

Early predictions of mechanical failure on surfaces that roughen randomly will be beneficial to several fields including Dentistry [4, 5], Micro/NanoElectro-Mechanics [6, 7, 8], Coatings [16, 39, 40], Mineralogy [41, 42], etc. In the field of Dentistry, it has been strongly emphasized the effects that surface topology has

Fig. 1.2- Fractured denture

on the life of oral prosthesis. For example, from the dental laboratory perspective, one of the 4 most common causes of fractures in implant-supported removable dentures (see figure 1.2) is roughness and wear of the posterior teeth to the point of loss of vertical dimension of occlusion resulting in anterior teeth fracture/debonding [5].

Much study has been done trying to characterize and predict the influence of roughness on Micro/Nano Electromechanical devices. For example, the influence of random roughness on cantilever sensitivity and resonance frequency has recently been studied [6,7] and cantilever Bending with rough surfaces was previously well studied by Jorg Weissmuller et al., who concluded that roughness has a non-negligible effect on the cantilever sensitivity [8].

Fig. 1.3- Failure coating films

Failure of coating films (figure 1.3) takes place after the loss in barrier integrity due to the accumulated damage of small scale weather-induced degradation events. These events imprint a random rough damage on the coating surface, and, under some type of loading, it leads to chain scission, and then probably, to coating fracture [18]. A hefty number of investors have obvious interest in predicting the service life of polymeric products exposed to the environment, as these represent, for example, the protective coatings of many structures in service [32]. It has been found that the cracks in the coating of gas turbine blades act as an initiator for the thermal fatigue crack [31]. Economical and safety reasons are among the

most important benefits to gain from more accurate service life predictions of coatings [32]. These needs are more extensively expressed in a symposium entitled "Service Life Prediction" [9], which for the sake of conciseness of the present work, have been left to the choice of the reader.

1.4 Background and Proposed Study

Ever since the awakening of fracture mechanics in the 1950's, much study has been carried out to try to correlate structure failure with different geometrical discontinuities and singularities, and relationships for, in particular, stress concentration factor, K_t, are widely known for these [1,13,17, 18]. Moreover, with the advent, and continuous refinement, of Finite Element Modeling (FEM) much more complex geometries and customized problems have been able to be resolved and predict failure accurately [33, 34,35]. Tada, Paris and Irwin made an important contribution of 30 years of work on developing and compiling a comprehensive source of formula and stress analysis information on crack problems, particularly for very specific geometric flaw shapes and periodic patterns [10]. Howbeit, understanding of surfaces with randomly concentrated pits of ablation and their correlation to material properties need still much study [43, 44]. Moreover, in comparison to fracture of metals, research of the behavior of fracture for nonmetals, is not still mature, whose understanding is vital to optimizing applications for the aforementioned fields [38, 18].

Now, as far as what type of surfaces should be considered, it is clear [22] that many surfaces are non-Gaussian; but it is equally clear that many surfaces are Gaussian [22].

More importantly, a study of Gaussian surfaces should give a preparatory background for the study of non-Gaussian surfaces [12].

Therefore, since constitutive models for deformation of amorphous material failure have been developed for fracture of well defined notches, the present study couples both experimental, statistical theory and finite element simulation to extend knowledge of materials failure by fracture, from initial service surface conditions and during random surface damage accumulation and environmental degradation. In practical terms, this endeavor is attempted by means of correlating profile and surface statistical parameters [23, 24, 25] of a dynamic surface that moves from a “flat” manufactured [21] to a Half Gaussian and, finally, to a Full Gaussian (early stages of wear) with respect to fracture location probabilities.

Chapter 2 Methodology

Like in any engineering design, selection of processes, materials, dimensions, functional limitations, and resources are all interconnected and strictly related. Therefore, a proper algorithm to select a process must keep in mind, for instance, a type of material and the dimensions required, and so on, see figure 2.1. Following are the Material, Dimensions and Process used in this study, while keeping functionality and standard testing in mind.

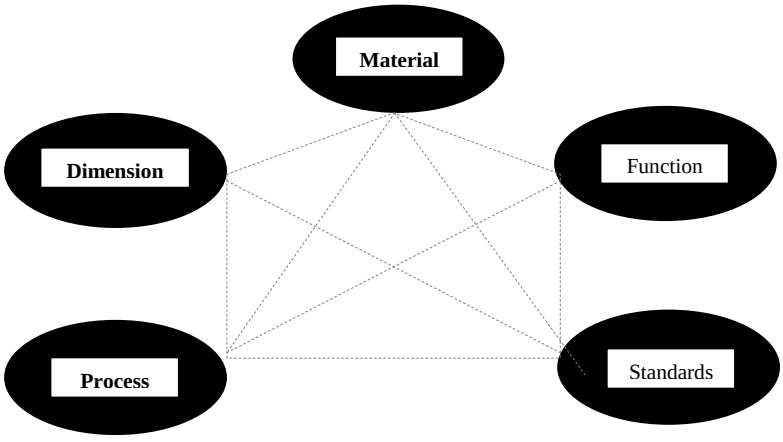

Fig. 2.1- Algorithm to select the different aspects of the methodology

2.1 Material Selection

Random rough surfaces were to be mathematically modeled, and repeatedly developed on specimens through a method that generated reproducibility on the mechanical properties of the samples. Therefore, the challenges of selecting the proper material for this study stemmed from the following needs:

- A material that could be easily ablated without causing secondary chemical and/or physical effects on the surface.

- A material that could macroscopically be flat enough, in order to differ from the rather light damage that would be imprinted on it.
- A material that would allow temperature to vary it from brittle to ductile, for future further study.
- A material that could be mechanically tested with standard test procedures.
- A material that could be made into the needed dimensions.

The material selected was commercial Methyl Meth-Acrylate (PMMA) polymer (figure 2.2b) made by Plaskolite and containing 99.5% Poly Methyl Methacrylate and 0.5% Methyl Methacrylate. Sheets of this material were purchased having dimensions of 36 inches by 72 inches wide by 0.118 inches thick (figure 2.2a). Values of modulus and stress and strain at fracture were found through experimental procedures. Bending tests at room temperature and 0.2 in/min strain rate were carried out using an MTS (Insight 30) machine, graphs of which are sown in figure 2.2c-d. For a set of 10 samples, the average Elongation at break was 2.7% with a standard deviation of 0.4%, and the modulus was 2.2 GPa.

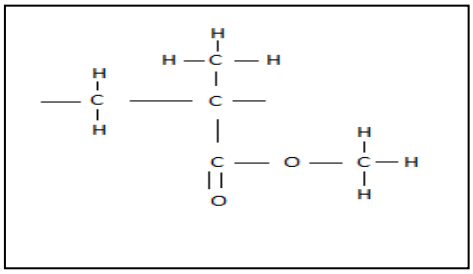

Fig. 2.2 (a)-Sheets of PPMA. (b)- Repeating Unit (Mer) of Polymer selected

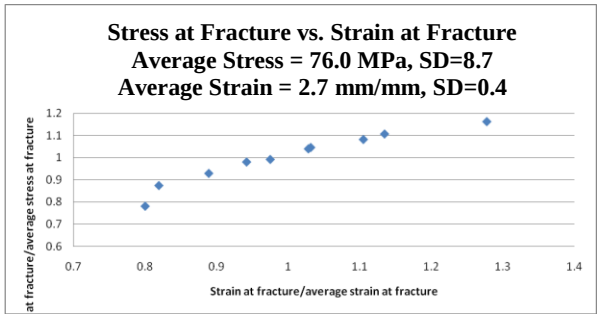

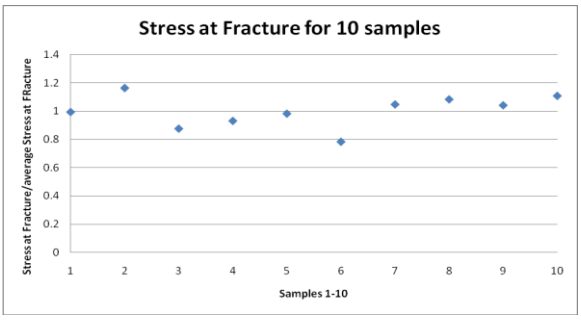

Fig. 2.2 (c)-Stress vs. Strain at Fracture for Acrylic selected. (d)- Stress at Fracture for 10 standard (flat) samples

2.2 Dimensions

2.2.1 Overall Dimensions

Unless otherwise specified, for all the experiments carried out in this study, the dimensions used (based on ASTM D 790 Standard Test Methods for Flexural Properties of

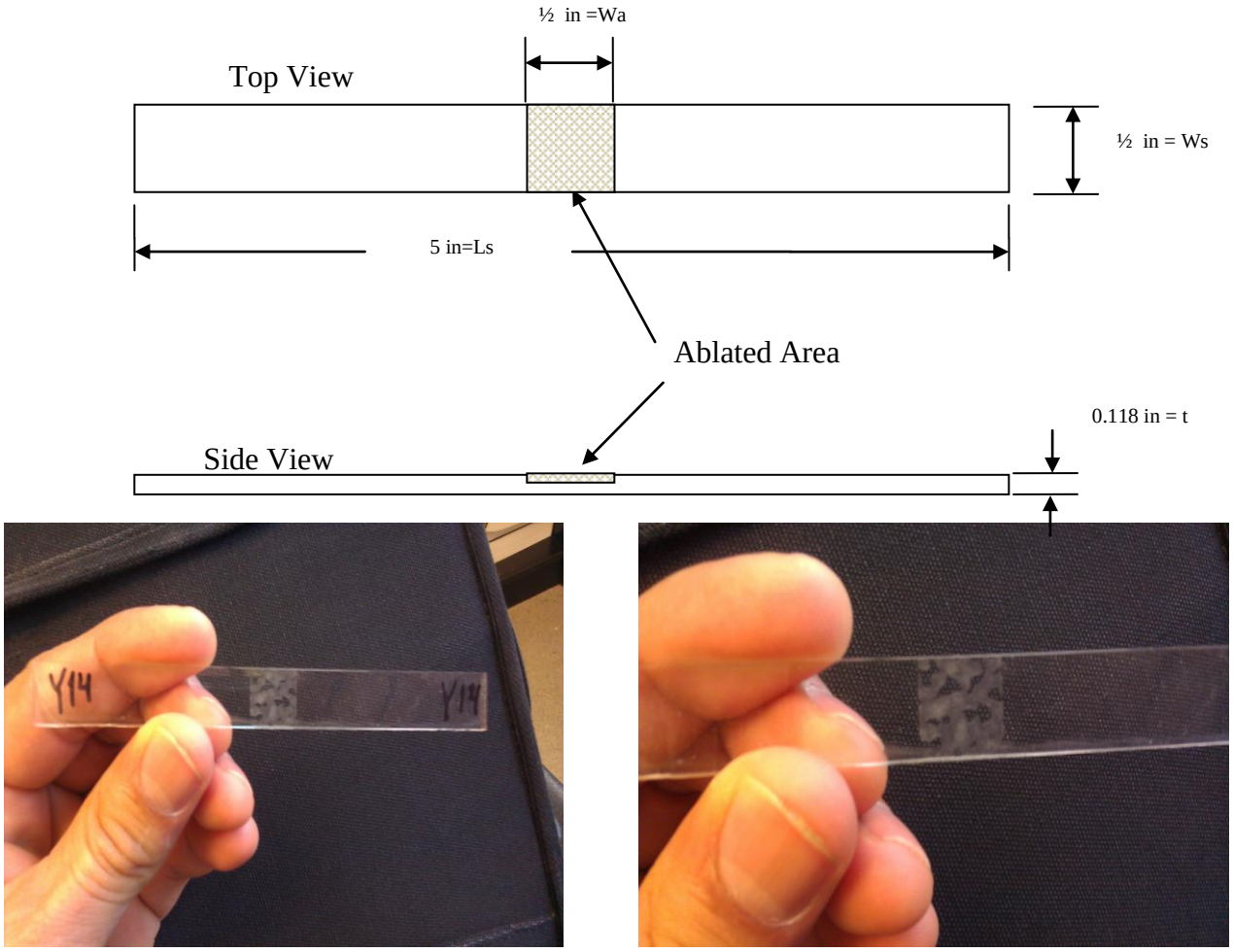

Fig. 2.3 (a,b)-Dimensions of specimen: (a)Top view, (b) Side View. (c,d)- Actual photos of specimens

Unreinforced and Reinforced Plastics and Electrical Insulating Materials), including for the tests in the aforementioned section, are those shown in figure 2.3. Note that thickness of the ablated area is highly exaggerated on that schematic.

Actual depth of the damaged region is in the order of the thousandths of specimen's total thickness, which in absolute terms is in the range of 2 to 60 micrometers approximately.

2.2.2 Ablated Region Dimensions

Two parameters were used to develop a whole spectrum of random rough surfaces, namely, Auto Correlation Length (ACL) and Deepening Step (D). ACL is defined as a surface roughness parameter that provides spatial information of surface topography that is not included in amplitude parameters such as root-mean-square roughness. In relation to the Auto Correlation Function (ACF), the ACL is defined as the length over which the

ACL (micrometers)	Wa=Ws=W (mm)	ACL/W(pcm)
10	12.7	78.7
30	12.7	236.2
45	12.7	354.3
60	12.7	472.4
90	12.7	708.7

Table 2.1- Some of the used values for Auto Correlation Length compared to Total ablated dimensions.

former drops to a small fraction of its value at the origin, typically 10% of its original value. Much information about the randomness of a surface can be understood from its ACL. The degree of randomness of a surface increases with an increase in the magnitude of its ACL.

Some values of ACL/W (where W=Ws=Wa=0.5 inches) are shown in table 2.1. Note that the units are in metric and that of ACL/W is in percent mille (pcm).

Deepening is intended to emulate the dynamic increase of surface damage into the bulk of the material. As it will be explained in more detail in chapter three, initially the surface is half Gaussian (HG) and it grows into an approximately full Gaussian (FG) surface. Deeper surfaces (D>45) were also studied in order to verify that, as surface damage becomes large enough, the behavior is similar to what traditional models predict (i.e. Griffith's crack criterion, provided that the several flaws are approximated as a single average one). The process of deepening was chosen to be a linear one, mostly because this

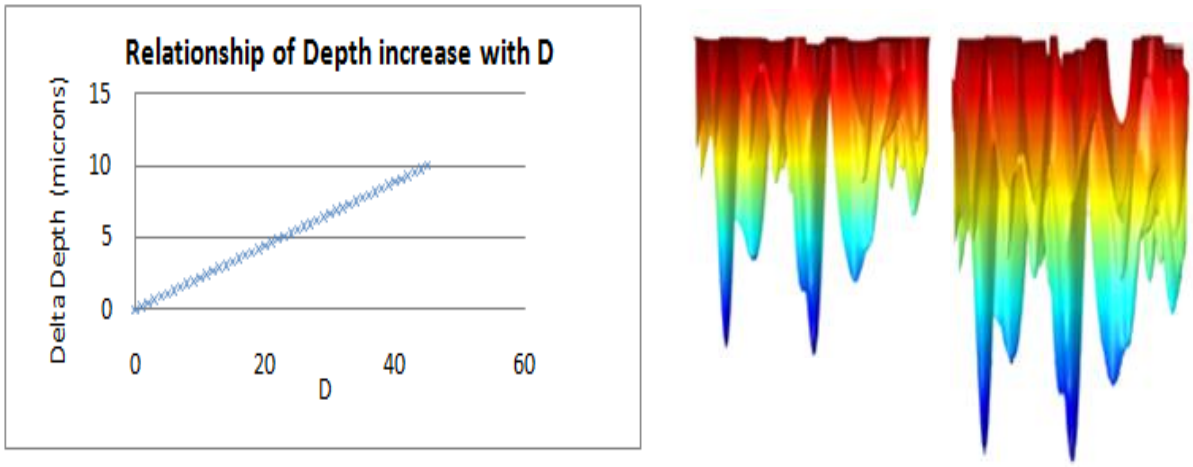

Fig. 2.4: a) Empirical correlation relationship between deepening parameter, D and RTD.
b) Plots of (left) D=0 (HG) surface and (right) D=45 (FG) surface. Both surfaces developed with ACL=45

study is more concern with the end stages as supposed to the paths themselves. Moreover, since the steps of deepening considered are rather fine, the process could accurately simulate a continuous one. A deepening step zero (D=0) represents an initial HG surface, while D=45 represents a FG surface. Now, since the process of Laser development (see

section 2.3.1) required calibration for the acrylic used, a relationship of true depth versus D needed to be developed, which in fact is shown in figure 2.4a. So, for example, D=45 (FG surface) represents an increase of about 10 micrometers from the initial surface (D=0). For the sake of comparison, figure 2.4b shows "D=0" and "D=45" surfaces developed using ACL=45. Also, Table 2.2 shows some of the values of D used compared to the overall thickness of the specimens. Included in that table are values of the corresponding Relative True Depth (RTD) which is the true distance, in micrometers, with respect to the initial HG surface. Maximum Absolute True Depth (ATD) values for a FG surface are around 45 micrometers, which represent about 15 thousandths of the specimen's total thickness.

D (steps)	RTD (micrometers)	RTD/t (thousandths)
0	0	0
15	3.33	1.11
30	6.67	2.22
45	10	3.33

Table 2.2 Some of the used values for D and the corresponding RTD, and ratio RTD over specimen thickness.

2.3 Experimental Process

The entire process followed in this study has been depicted in the Procedure Flow Diagram shown in figure 2.5. This chapter will cover the experimental part of the process, i.e. laser ablation/cutting, profiling measurements, Mechanical Testing and High Resolution Scanning photographing, leaving the Mathematical Model part for chapter 3 and Measurements and Analysis for chapter 4.

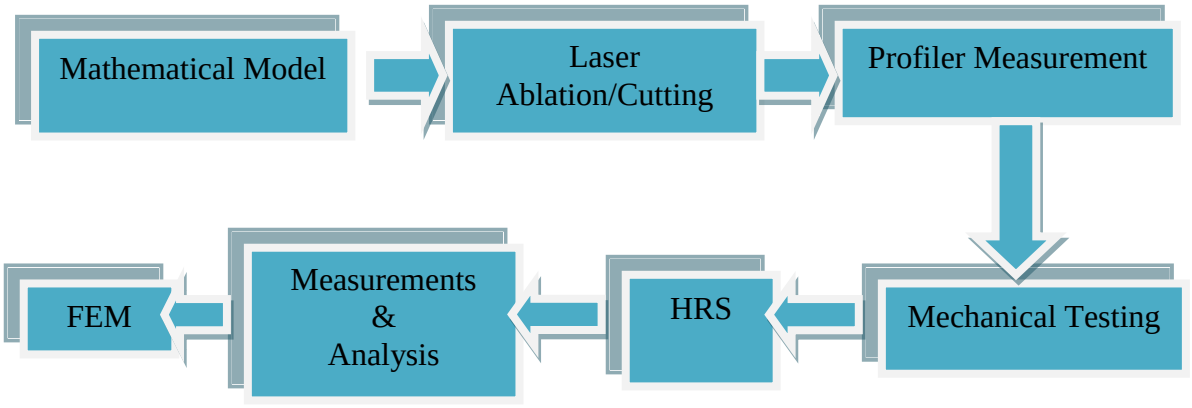

Fig. 2.5 Entire Procedure Flow Diagram of Study

2.3.1 Laser Ablation/Cutting

2.3.1.1 Laser System

Fig. 2.6- CO_2 based laser system used to cut and ablate acrylic shims.

After the random surfaces were mathematically modeled and digitally developed by making use of the Direct Convolution Method (DCM) developed by Bergstrom (see chapter 3), via a Matlab code, these were vector-cut and 3-D engraved. A laser machine of the type Mini Epilog 30 watt (figure 2.6) was utilized for this part of the process, this equipment uses CO_2, with a resolution of 10 microns. This spot size resolution is

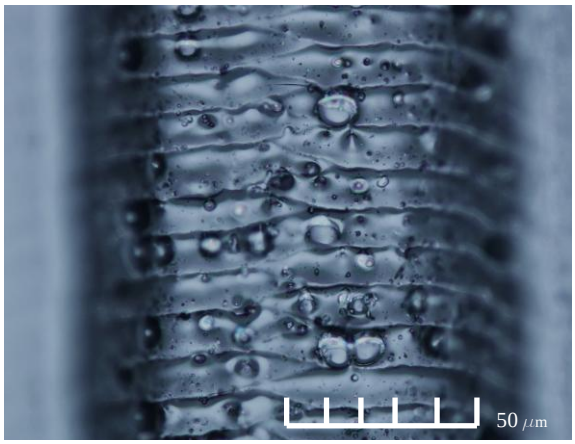

Fig. 2.7- Micrograph of ablated PMMA proving the manufacturer's claim of Laser's resolution = 10 microns.

precisely the reason why the minimum ACL of 10 was selected, since lower ACL would not have been able to be accurately reproduced by this device.

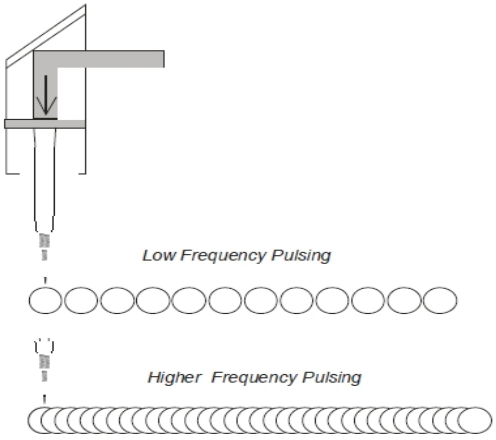

Fig. 2.8- Contrast of Low and High Frequency modes

Shown in figure 2.7 is a micrograph of the smallest features obtained with this CO_2 system. Note the wavelength of about 10 microns etched. Also note the tiny circular shaped features produced by sparks which would be non negligible if ACL was below 10 micrometers. Also, it is important to mention that high frequency mode was selected in order to obtain higher fine-resolution output. Figure 2.8 shows a sketch of the difference between low and high frequency modes. Note for instance that, for cutting, low frequencies produce a perforation as opposed to the continuous cut obtained with high frequencies pulsing.

2.3.1.2 Calibration

Since depth's output and resolution depends strictly on the particular application and

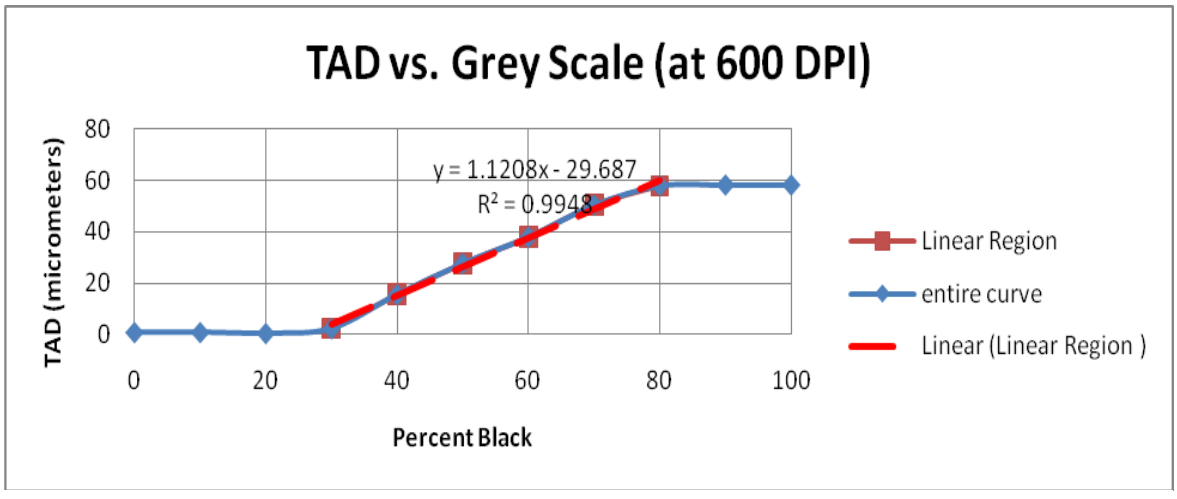

Fig. 2.9- True Ablated Depth versus Grey Scale non linear curve, and Linear Portion taken from it.

material used, calibration needed to be carried out in order to correlate the digitally developed grayscale bitmaps (representing rough surfaces) with True Ablated Depth (TAD). Calibration was performed using 600 dots per inch resolution on the laser printing specifications. This value was consistently used throughout the procedure and experiments, as well. A feature called 3-D engraving was used for the experiments. This laser feature understands grayscale in a way shown by the graph of figure 2.9. As it can be noticed, the curve is non linear and possesses an "S" shape, approximately. However, for Percent Black (PB) of between 30 to 80% the curve behaves rather linearly. A least squared fit was carried out to find a relationship between TAD and PB, which resulted in:

$$TAD = 1.1208 * PB - 29.687 \quad \textbf{(eq. 2.1)}$$

With a Coefficient of Determination, R^2=0.9948. Equation 2.1 was used in combination with the procedure to be shown in chapter 3, in order to transform properly to the surface-grayscale bitmaps developed using the mathematical model.

2.3.2 Profile Measurements

Profile measurements were carried out using an XP Stylus Profiler, which is a

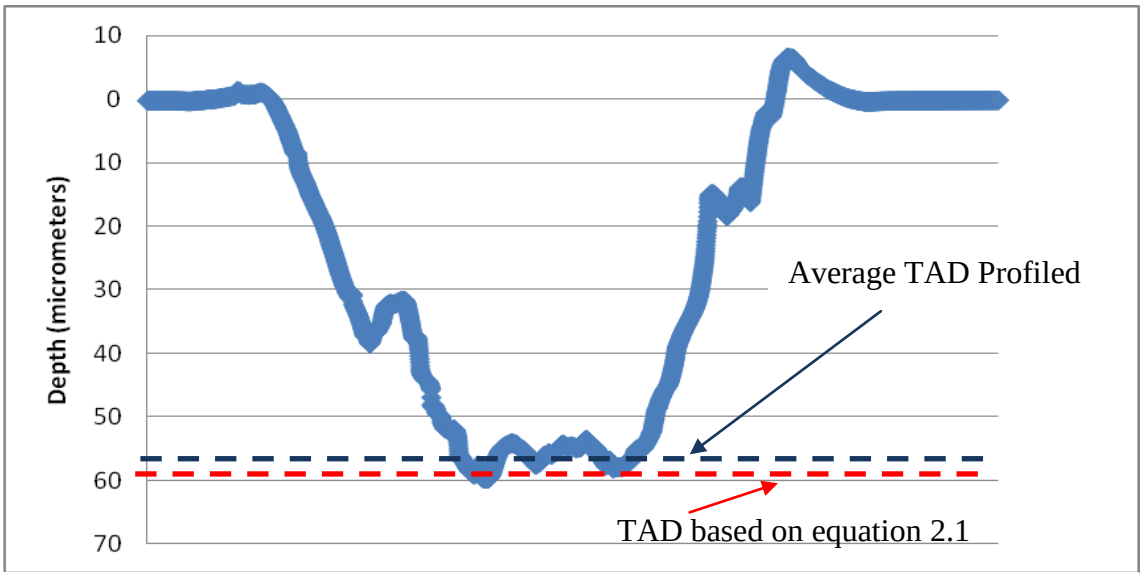

Fig. 2.10- Profile showing TAD compared to that obtained from equation 2.1

computerized, high-sensitivity surface profiler that measure roughness, waviness, and step height in a variety of applications. It features the ability to measure precision step heights from under 10 Å to as large as 100 microns and provides more than five orders of magnitude of precision Z height measurements.

Laser-ablated samples were profiled in order to compare the precision of our process combined with the accuracy of equation 2.1. Figure 2.10 shows an actual scanned profile. It also shows the average TAD that was etched with CO_2 laser system used and how it compares with the target TAD predicted by empirical equation 2.1. The difference lies between 3-5%, which represents about 2-3 micrometers of true depth in average.

2.3.3 Mechanical Tests

PMMA beams having dimensions shown in figure 2.3 were bent using standard ASTM D790 3-Point Bending Tests using an MTS machine, as depicted in figure 2.11. The Test parameters are shown in table 2.3. It is important to notice the value of the strain rate as it is one of the major parameters that affects the mechanical behavior of polymers. Also, all

Fig. 2.11- One of the D790 3-point ASTM standard Bending test performed.

tests were performed at around 20 degrees Celsius which is well below the Glassy-to-Leathery transition temperature for PMMA. This is evidently proved by a simple comparison of the stress-strain curves obtained, figure 2.12a, with graphs produced by T.S.

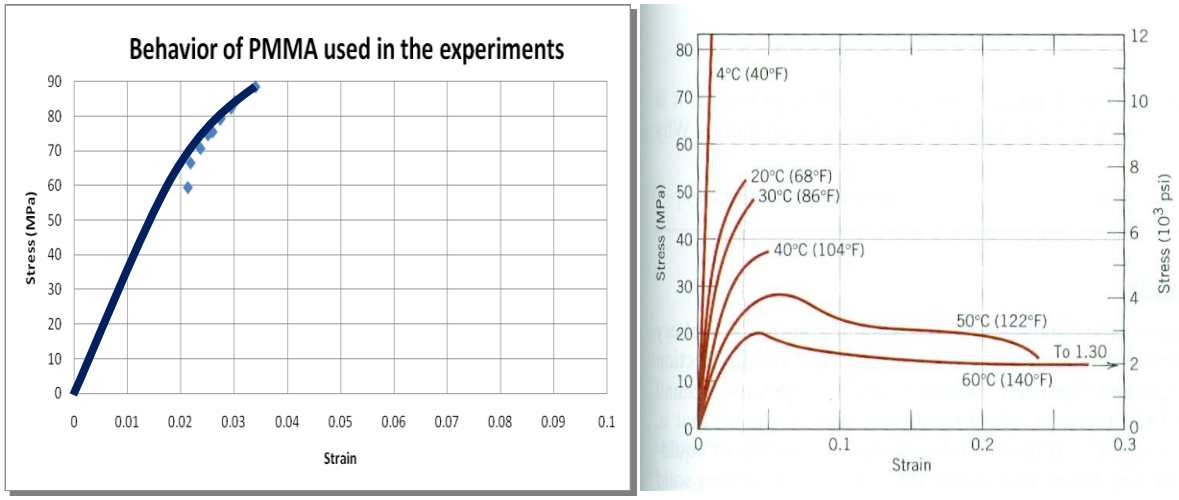

Fig. 2.12- (a) PMMA mechanical **bending** behavior from present study; (b) PMMA mechanical **tensile** behavior from experiments reported by ASTM (Carswell and Nason 1944)

Carswell and H.K. Nason and published by ASTM [19], which is shown in figure 2.12b. This latter curve was developed from tensile tests, which explains why the moduli appear to have different values (one is flexural modulus and the other is Young's modulus of elasticity). What wanted to be emphasized is the similar mechanical behavior under similar temperatures.

Parameters	Value
Strain Rate	0.2 in/min
Span length	3 inches
Thickness	0.118 inches
Width	0.5 inches

Table 2.3- Parameters and values used in the 3-point bending tests

An array of various values of ACL and D led to a total of 90 types of repeatable rough surface specimens to be bent. Moreover, 10 different random roughnesses were developed which totals 900 types of specimens, not all of which were bent. Figure 2.13 shows a photo of a small portion of the roughened acrylic specimens after bending-to-fracture tests were performed on them.

Fig. 2.13- Portion of sets of already-broken specimens

2.3.4 High Resolution Scanning (HRS)

After specimens were bent to fracture, HRS was performed to sets of them in order to digitally measure fracture locations. It might be worthwhile mentioning that this was also done in order to compare the top view aspect of the digitally-developed grayscale-bitmap surface with the actual laser-ablated ones, which is shown in figure 2.14. (Recall that comparison of depth was discussed in section 2.3.2). HRS was performed using an HP Scanjet G4050 device; scans were saved into Tagged Image File Format (tiff) files with an output resolution of 1200 pixels per inch (PPI). Notice in figure 2.14 that while on the gray scale plot, darker means deeper, on the actual HRS photos lighter color means deeper.

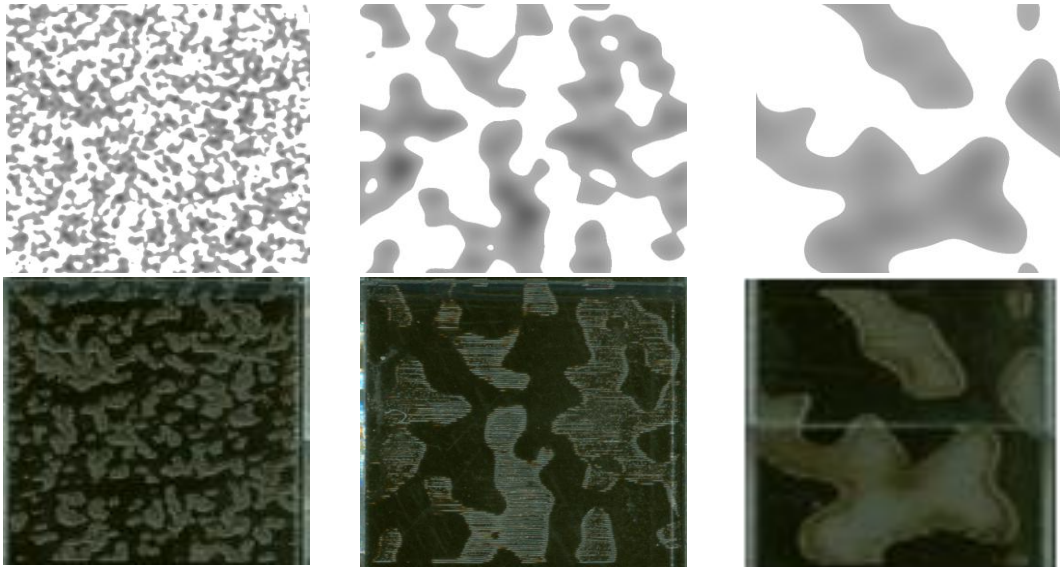

Fig. 2.14- Matrices plots (top) and HRS pictures of actual shims (bottom) for, (a) ACL=10 microns, (b) ACL=45 microns, (c) 90 microns.

As mentioned before, in developing our specimens ACL was varied from 10 to 90 in steps of 10, which infers 9 values for ACL (N_{ACL}=9). Also, D was varied from 0 (HG) to 45 (FG) in steps of 5, which means 10 values of D (N_D=10). Additionally, random surfaces were developed 10 times, therefore having 10 different types of random models (N_{RR}=10). This means that, N_{ACL}* N_D* N_{RR}= 900 types specimens were digitally developed for the present study. Furthermore, for each type of digitally-developed specimen, 14 specimens (Ns=14) were laser-ablated, two of which were kept (not bent) for other study purposes. Only strategic types of specimens were needed in order to cover the entire spectrum of the scope of this study. So, selection was made for ACL=10, 45, 90; likewise, D=0, 15, 30, 45. Higher values of D, 90 and 135 were also studied. These were laser-developed twice (and for some types of specimens even three times) in order to confirm results. Figure 2.15 shows HRS photos for ACL=10, 45 and 90, and D=0, 15, 30, and 45, for 12 specimens. Each one of the three blocks is a type of ACL with D increasing downwards.

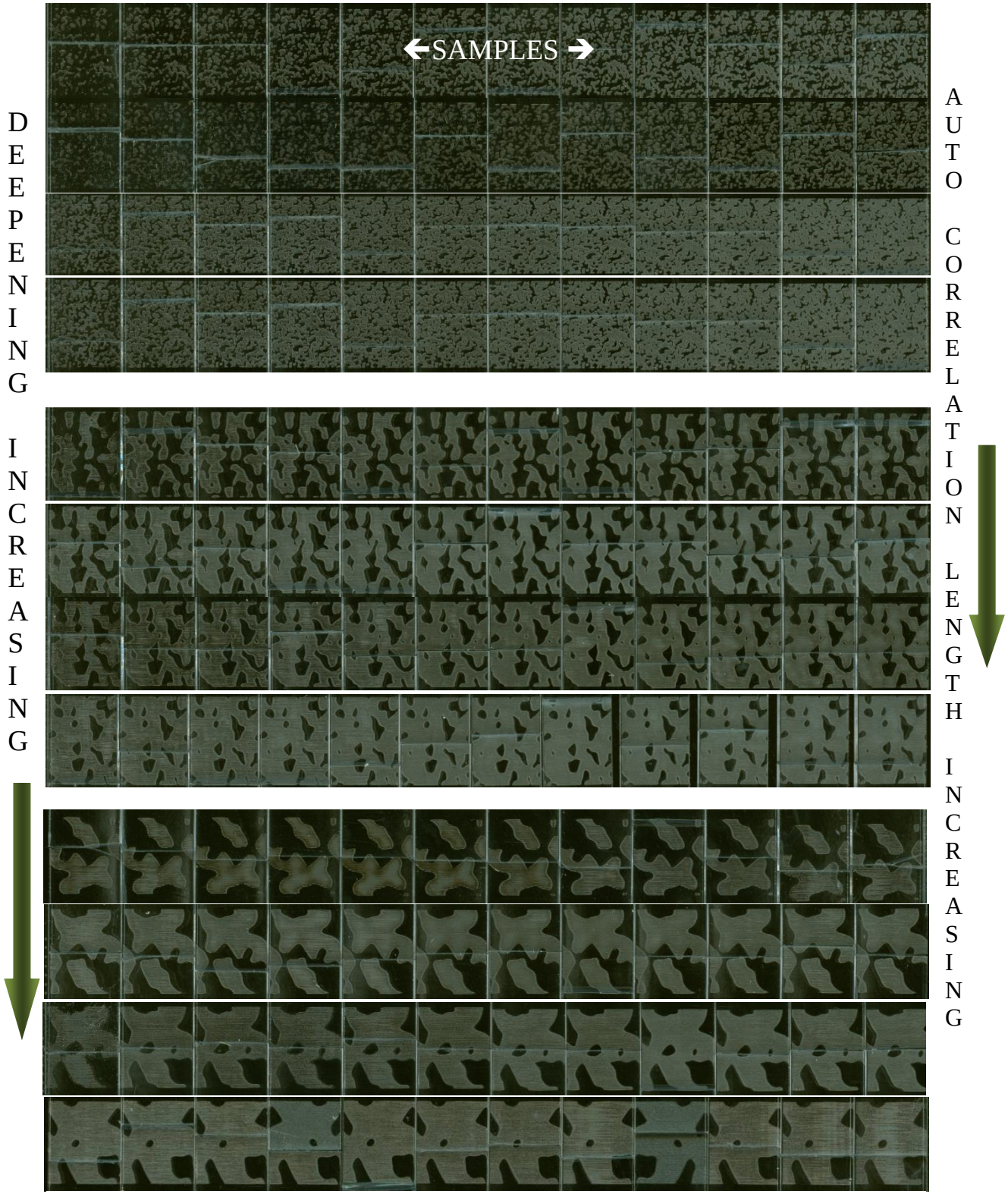

Fig. 2.15- HRS photos of 144 specimens. Upper Block: ACL=10, Middle Block: ACL=45, Lower Block: ACL=90. At each block there are 4 lines of specimens. Each line corresponds to a different value of D, increasing downward. D=0, 15, 30, and 45.

CHAPTER 3 Mathematical Model

This chapter covers the reasons for and the actual process of the mathematical model used to develop the random rough surfaces and simulation of the dynamic degradation process.

3.1 Central Limit Theorem and Convolution

Natural weathering and wear of structural materials in service nearly always generate surface roughness, as weathering is an accumulation of vast numbers of small, random assaults and thus follows the Central Limit Theorem (CLT) prediction for surface topology. CLT explains the behavior of the sum of random variables. One of the most commonly used forms of the theorem is as follows. Let $Z_1 \ldots Z_n$ be random variables with sum, $S = \sum_{k=1}^{n} Z_k$, then CLT predicts that the S will have a Gaussian distribution provided that:

1. Each summand that is not negligible compared to the dispersion of the entire sum has a distribution close to Gaussian.
2. The maximum of the absolute value of the negligible summands is itself negligible compared to the dispersion of the sum.

And, since convolution is directly related to the probability distribution of S, then what is being said, in basic terms, is that a random signal (in our case, a random surface), or whatever other signal, when it is convoluted by itself several times, it grows very rapidly

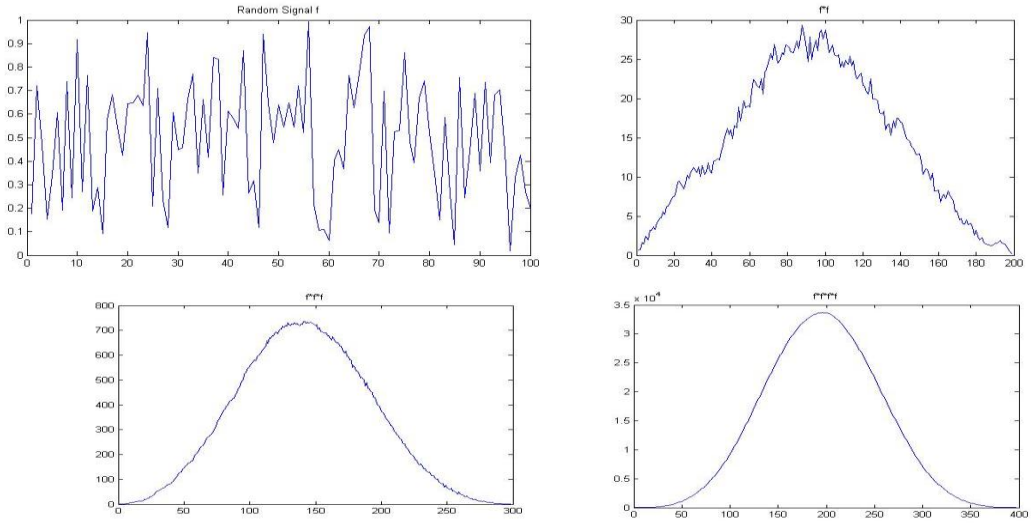

Fig. 3.1- A visual prove of how a random surface (or signal) when convoluted by itself grows into Gaussian. Notice that it only takes 4 convolutions to clearly see "bell-shape" Gaussian distribution.

into a Gaussian distribution. A simple code to show this fact is depicted in figure 3.1. The first graph is a randomly generated signal, called f; the second graph is the convolution of f by itself; the third and fourth are the convolution of f 3 and 4 times, respectively. As it can clearly be seen, normal distribution is attained rather quickly. So our approach consists on developing a random rough surface with Gaussian behavior, which signifies the final surface, and "pushing" it into an ideally perfect surface, step by step, as though imitating, for instance, a natural weathering process, as depicted in figure 3.2. In our case, the process will start with a Half Gaussian (HG) surface and ends with Full Gaussian (FG) one.

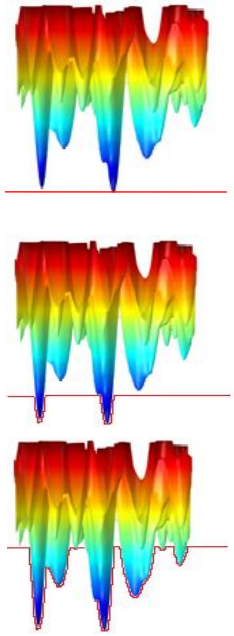

Fig. 3.2 "Pushing in" a Gaussian Surface

Now, it is well known that if a distribution follows the Gaussian (also called normal) behavior, then its probability distribution function is:

$$P(x) = \frac{1}{\sigma\sqrt{2\pi}} e^{-\frac{(x-\mu)^2}{2\sigma^2}} \quad \text{On the domain } (-\infty,\infty) \qquad (\textbf{eq. 3.1})$$

Where σ is the Standard Deviation and μ is the mean. Commonly (3.1) is normalized by taking μ=0 and σ^2=1. Or a change of variable is performed on (3.1) using,

$$Z = \frac{(x-\mu)}{\sigma} \qquad \textbf{(eq. 3.2)}$$

Carrying out this change of variables, one gets:

$$P(x)dx = \frac{1}{\sqrt{2\pi}} e^{-\frac{z^2}{2}} dz \qquad \textbf{(eq. 3.3)}$$

(This rescales the roughness).

3.2 Random Rough Surface Generation

For this study, random surfaces were generated using a pseudo random generating function, Random(x), in Matlab®), that utilizes a multi-seed approach and it can generate up to 2^{1492} numbers before repeating itself [20].

Let the depth of the surface be a function of x and y, according to the coordinate system shown in figure 3.3, such that,

$$z(x,y) = \sigma \cdot Random(x,y) \qquad \textbf{(eq. 3.4)}$$

Which implies that z is a random (normally distributed) variable with mean zero and standard deviation, σ. Assuming isotropy in the x-y plane, then we defined the Gaussian filter f as,

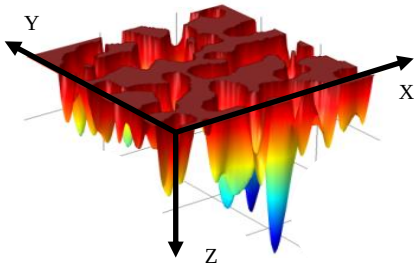

Fig.3.3-Rectangular coordinate system with respect to a surface

$$f(x,y,ACL) = e^{-\frac{r^2}{ACL^2}} \qquad \textbf{(eq. 3.5)}$$

Where $r(x,y) = \sqrt{x^2+y^2}$ **(eq. 3.6)**

Applying the Direct Convolution Method, DCM, [11]:

$$Fbergstrom = \frac{2}{\sqrt{\pi} \cdot N \cdot ACL} L \cdot \frac{1}{N} \sum_{k=0}^{N-1} [DFT(z) \cdot DFT(f)] \cdot e^{\frac{i2\pi kn}{N}} \qquad \textbf{(eq. 3.7)}$$

Where N= number of grids along each axis. (N=600 was used)

ACL=auto correlation length (varied from 10 to 90, in steps of 10)

L: for this application, L=N

DFT is the Discrete Fourier Transform, so in eq. 3.7, the two expressions can be written as,

$$DFT(z) = \sum_{n=0}^{N} z(n) \cdot e^{\frac{-i2\pi kn}{N}} \qquad \textbf{(eq. 3.8)}$$

And similarly,

$$DFT(f) = \sum_{n=0}^{N} f(n) \cdot e^{\frac{-i2\pi kn}{N}} \qquad \textbf{(eq. 3.9)}$$

A Matlab code called “Raw Arrays” that carries out all these calculations is shown in Appendix A.

3.3 Surface Truncation and Replacement

Next, the Gaussian surface is truncated and replace back by taking the average location and only including values below that average. D=0 stands for complete truncation and no replacement; D=5, 10, and 15 represent 5, 10, 15 points, respectively, of replacement of surface after truncation. A simple pseudo code, representing that, follows:

```
    For D=0 until 45 by steps of 5
        fBergstrom(i)=fBergstrom+D;
For all i
```

```
Surface(i)=(fBergstrom(i)>0).*fBergstrom(i);
```

Next, normalization and some transformations of the arrays were carried out for three main reasons:

1. Grayscale was to be used to interpret depth,
2. The linear section of the gray scale in figure 2.9 goes from 30-80%,and
3. The program language used (Matlab) interprets 0 (zero) as 100% black and 1 (unity) as 100% white.

To explain this more clearly, an example could be rather useful. Let A be a matrix produced by the code "Raw Arrays". Notice, that it is clear from the values shown after eq. 3.7 that "Raw Arrays" produces Arrays having dimensions of 600 columns by 600 rows. So, let A be a 600x600 array such that,

$$A=\begin{bmatrix} 45 & 0 & 255 & 255 & 45 & . & . & . \\ 12 & 201 & 223 & 85 & 90 & . & . & . \\ 60 & 75 & 56 & 100 & 111 & . & . & . \\ 23 & 255 & 89 & 0 & 55 & . & . & . \\ 190 & 167 & 34 & 134 & 99 & . & . & . \\ . & . & . & . & . & . & . & . \\ . & . & . & . & . & . & . & . \\ . & . & . & . & . & . & . & . \end{bmatrix}$$

After normalization, A becomes B, by dividing by 255:

$$B=\begin{bmatrix} .176 & 0 & 1 & 1 & .176 & . & . & . \\ .047 & .788 & .875 & .333 & .353 & . & . & . \\ .235 & .294 & .220 & .392 & .435 & . & . & . \\ .090 & 1 & .349 & 0 & .216 & . & . & . \\ .745 & .655 & .133 & .525 & .388 & . & . & . \\ . & . & . & . & . & . & . & . \\ . & . & . & . & . & . & . & . \\ . & . & . & . & . & . & . & . \end{bmatrix}$$

Notice, that the maximum value is indeed 255, which represents 100% black and after normalization becomes 1 (unity). However, as it was mentioned before, the programming language used (Matlab) interprets unity as 0% black; so, a proper transformation is needed, which leads to C:

$$C = \begin{bmatrix} .824 & 1 & 0 & 0 & .824 & . & . & . \\ .953 & .212 & .125 & .667 & .647 & . & . & . \\ .765 & .706 & .780 & .608 & .565 & . & . & . \\ .91 & 0 & .651 & 1 & .784 & . & . & . \\ .255 & .345 & .867 & .475 & .612 & . & . & . \\ . & . & . & . & . & . & . & . \\ . & . & . & . & . & . & . & . \\ . & . & . & . & . & . & . & . \end{bmatrix}$$

3.4 Grayscale Transformation

Finally, a second transformation (Matrix C to D) is needed to correct the values according the calibration relationship of grayscale versus real depth, discussed in Section 2.3.1.2. Values are rescaled between 30 percent and 80 percent black. So, if there is no ablation, the value is kept the same, but if is some ablation, this value is transformed using the equation from calibration. For example, total ablation (zero) is interpreted as 0.2, since this value is the greatest ablation that can be obtained within the linear region of the calibration curve, and very close to the absolute TAD.

It can easily be shown that,

$$D_{ij} = \begin{cases} 0.5C_{ij} + 0.2 & C_{ij} \neq 1 \\ 1 & C_{ij} \equiv 1 \end{cases} \qquad \textbf{(eq. 3.10)}$$

From this equation, it can be noticed that all entries of D $\in$ [0.2, 1], but there are no values in the interval [0.7, 1). As explained before, 0.2 must represent 100% black. So, using C from the aforementioned example, D will look like:

$$D = \begin{bmatrix} .612 & 1 & .2 & .2 & .612 & . & . & . \\ .677 & .306 & .263 & .534 & .524 & . & . & . \\ .583 & .553 & .590 & .504 & .483 & . & . & . \\ .655 & .2 & .523 & 1 & .592 & . & . & . \\ .328 & .373 & .634 & .438 & .506 & . & . & . \\ . & . & . & . & . & . & . & . \\ . & . & . & . & . & . & . & . \\ . & . & . & . & . & . & . & . \end{bmatrix}$$

Matrix D is ready for grayscale 2-D plot to be used in the 3-D engraving mode on the CO_2 laser machine. Some of these plots can be seen in figure 3.4 for several values of D and ACL.

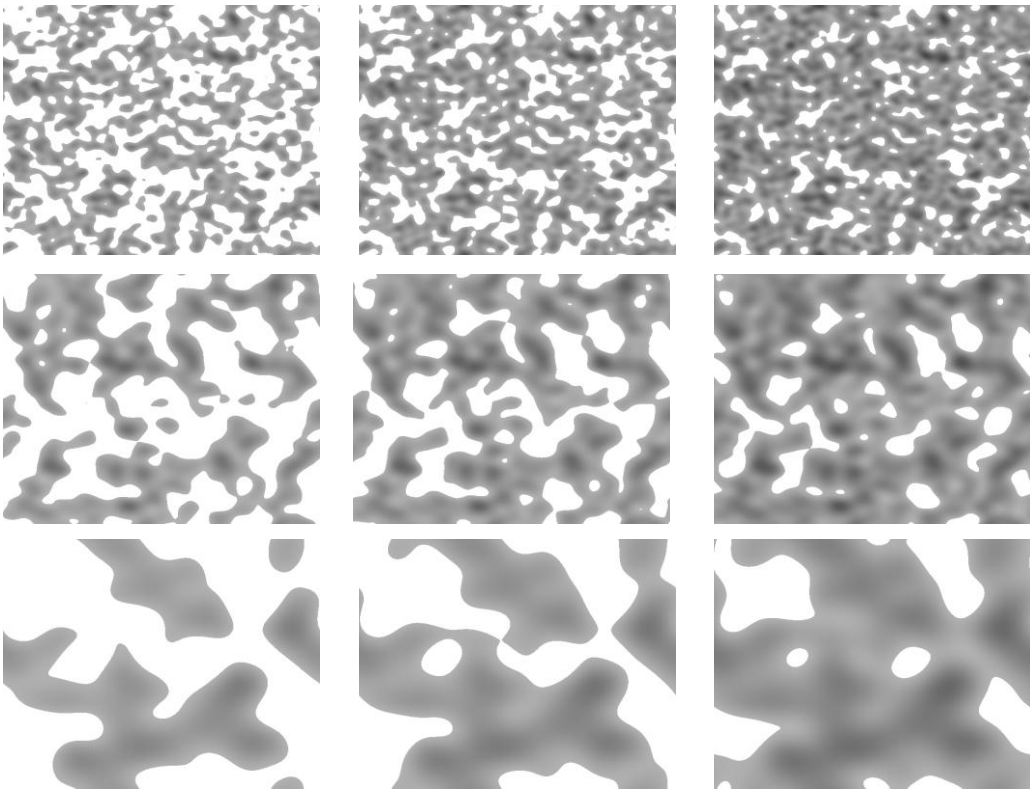

Fig. 3.4- Grey Scale Plots for (Up): ACL=15, (Middle): ACL=30, and (Bottom): ACL=75. From left to right D=0, 20, 45

3.5 Surface Transformation to xyz format

Even though Matrix D is ready for laser etching, however, it is not yet ready to be imported to a xyz datasheet to be used in statistical analysis and FEM. For this, yet another transformation needs to be carried out. The reason is, because D must be converted to TAD according to the results of equation 2.1. At this point, there are several approaches, depending on which matrix (A,B,C, or D) is to be transformed to TAD. For the sake of continuity of this process, it has been chosen to transform D into a TAD matrix, which will be called E.

Now, since the values of D are no longer those corresponding to x-axis of the plot of figure 2.9, a combined transformation must be performed to account for that. The result is a linear equation as following:

$$E_{ij} = \begin{cases} -115.78D_{ij} + 81.046 & D_{ij} \neq 1 \\ 0 & D_{ij} \equiv 1 \end{cases} \qquad \langle E_{ij} \rangle = \text{micrometers} \qquad \textbf{(eq. 3.11)}$$

This matrix E is ready to be imported into the Finite Element Modeling Software and also to be used to calculate the different statistical parameters for both overall surfaces and profiles. Also, and for the sake of completion, E has been calculated for the example above, and the result is as follows:

$$E = \begin{bmatrix} 10.2 & 0 & 57.9 & 57.9 & 10.2 & . & . & . \\ 3.82 & 45.6 & 50.6 & 19.2 & 20.4 & . & . & . \\ 13.5 & 17.0 & 12.7 & 22.7 & 25.1 & . & . & . \\ 5.2 & 57.9 & 20.5 & 0 & 12.5 & . & . & . \\ 43.1 & 37.9 & 7.6 & 30.3 & 22.5 & . & . & . \\ . & . & . & . & . & . & . & . \\ . & . & . & . & . & . & . & . \\ . & . & . & . & . & . & . & . \end{bmatrix} \text{ Micrometers}$$

Some surfaces coming from matrices of the type E are shown in figure 3.5. Notice that for each ACL and D, 3 different views are depicted.

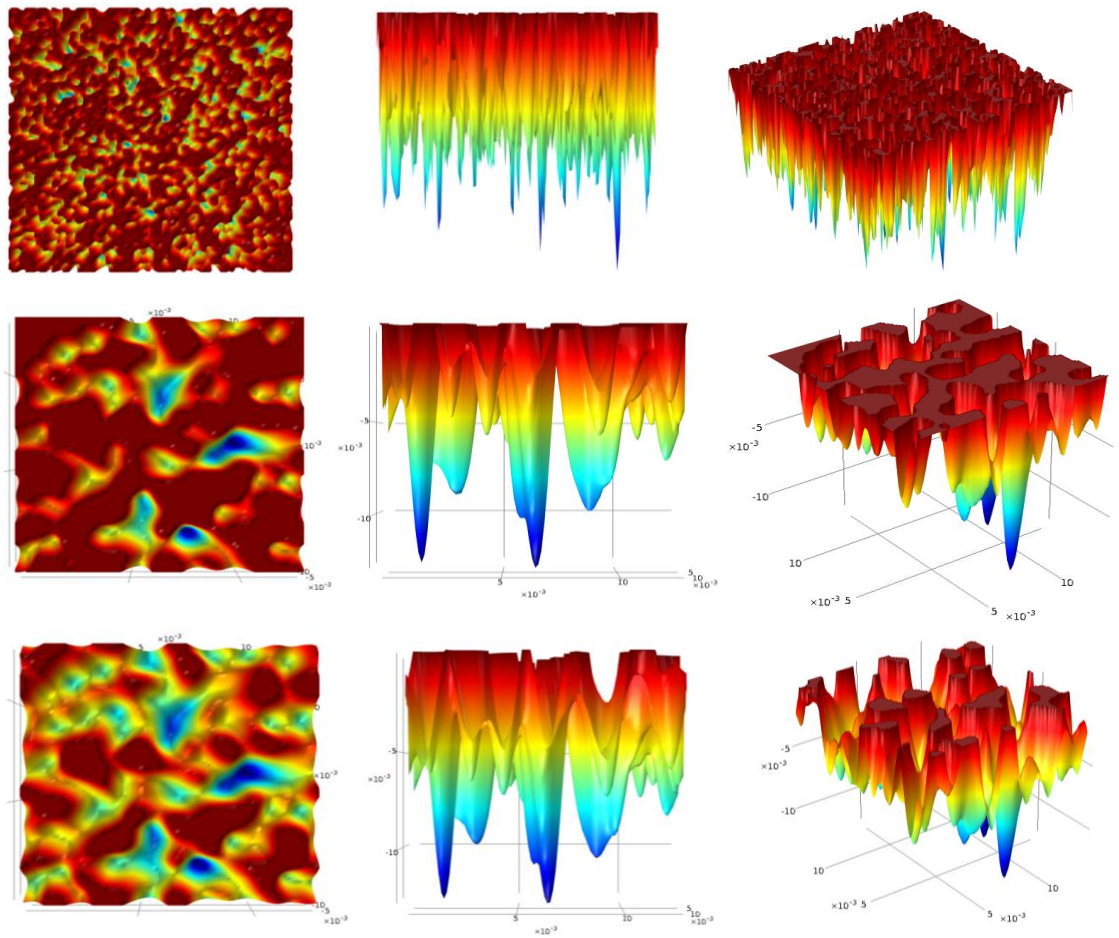

Fig. 3.5- Top, side and Perspective views of Surface Plots for (top): ACL=10, D=0; (middle): ACL=45, D=0; (bottom): ACL=45, D=45

3.6 Summary

So, in summary,

- The process simulated follows the Central Limit Theorem, and all the mathematical consequences of it.

- Gaussian Random rough Surfaces were developed using an exponential Auto Correlation Function (ACF)
- The Direct Convolution Method developed by Harald Bergstrom [11] was used to simulate the dynamic degradation process.
- Truncation of FG surface was performed and restoration was performed by steps.
- Computer Codes were developed to perform these lengthy calculations for 90 types of surfaces.
- Proper transformations of the arrays were carried out to account for how the laser system interprets gray scale, for TAD calibration, and for how the programming language interprets the grey scale.
- Arrays of surfaces were made ready and imported for both Statistical Analysis and FEM.

CHAPTER 4 Statistical Analysis

4.1 Fracture Mechanics

It has been known for a long time that the presence of discontinuities in a material, subject to a remote load, introduces stress concentrations which depend, to a great extent, on the geometry, location and orientation of the discontinuity with respect to the overall dimensions [1, 18]. The Stress Concentration Factor, K_t, is defined as the ratio of the local stress to the remote stress:

$$K_t = \frac{\sigma_{local}}{\sigma_{load}} \qquad \text{(eq. 4.1a)}$$

This implies that,

$$\sigma_{local} = K_t \sigma_{load} \qquad \text{(eq.4.1b)}$$

Fractures typically occur in locations where σ_{local} is high, see figure 4.1. In equation 4.1b, the stress in the right hand side is due to the bending caused by the load. However, the Stress Concentration Factor, K_t, is some type of function dependent on the roughness of the surface, which is exactly what this study is trying to investigate. It is proposed that K_t can be written as,

$$K_t(x, y) = \sum_{i=0}^{n} k_i F_i(x, y, i) \qquad \text{(eq. 4.1c)}$$

Where F(x, y, i) is some kind of polynomial function whose terms and respective exponents must be investigated. Also, k_i are constants of the series. Intuitively, it can be stated that F(x,y,i) is a function related to the different statistical parameters of the rough surface. For a given point (x,y) on the surface, the

greater K_t is, the higher the probability fracture will occur at that particular point. So focus will be made on the correlation between statistical surface parameters with fracture location probability.

4.2 Fracture Location Measurements

After *HRS* images were produced, these were used to measure the location of fracture, see figure 4.1. Let the function $\mathcal{H}(x_i)$ be the number of fractures that take place within a very small distance of the location corresponding to the line at x_i. And let $\mathcal{N}$ be the total number of fractures. So that, $\mathcal{H}(x_i)/\mathcal{N}$ can represent both density and/or the probability of fracture at location x_i. Then, $\mathcal{H}$ and hence, $\mathcal{H}/\mathcal{N}$ are directly proportional to K_t.

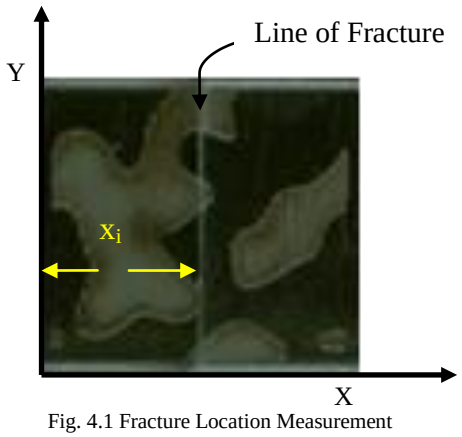

Fig. 4.1 Fracture Location Measurement

A plot of $\mathcal{H}(x, D)$ for ACL=45 is shown in figure 4.2. Notice that the long horizontal axis

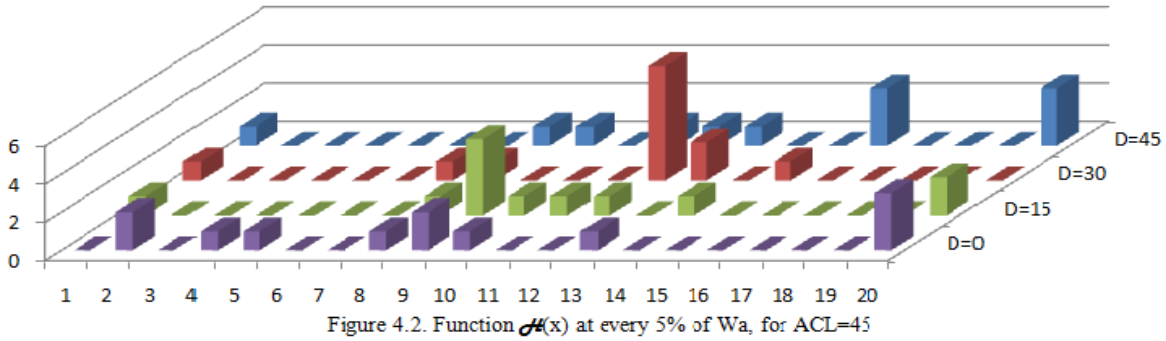

Figure 4.2. Function $\mathcal{H}(x)$ at every 5% of Wa, for ACL=45

in that plot represents location at every 5% of the total ablated width (W_a). Similar plots were developed for all specimens studied. Statistical calculations were performed for surfaces and profiles at every location x_i. Consider Figure 4.3, showing an actual cross-section profile at a particular location for initial and final conditions. Note that the y-axis of

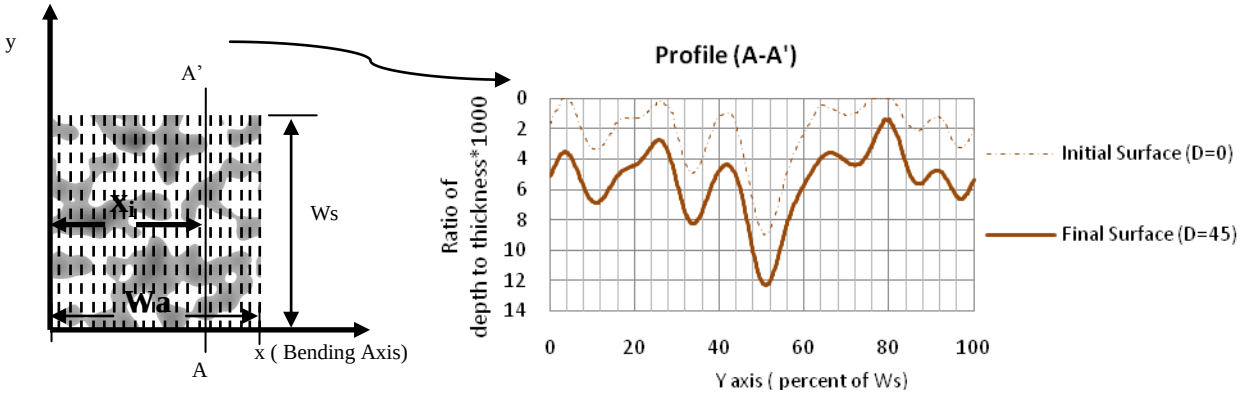

Fig. 4.3- (Left) Lines parallel to fracture locations, (right) Profile along some line at X_i, for D=0 and D=45

that profile plot is the ratio of TAD to total specimen thickness (t).

Statistical Analysis of the data obtained was performed considering the following parameters: average roughness, RMS roughness, variance, kurtosis, skewness, maximum depth, slope and curvature for both surfaces and profiles along lines parallel to fracture lines, see figure 4.3. So, statistical moments were evaluated using the following equations:

$$m = \frac{1}{N}\sum_{i=1}^{N} Z_i \qquad \textbf{(eq. 4.2a)}$$

$$R_a = \frac{1}{N}\sum_{i=1}^{N} |Z_i - m| \qquad \textbf{(eq. 4.2b)}$$

$$s^2 = \frac{1}{N}\sum_{i=1}^{N} (Z_i - m)^2 \qquad \textbf{(eq. 4.2c)}$$

$$Sk = \frac{1}{s^3 N}\sum_{i=1}^{N} (Z_i - m)^3 \qquad \textbf{(eq. 4.2d)}$$

$$R_q^{\,2} = \frac{1}{N}\sum_{i=1}^{N} (Z_i - m)^2 + (m)^2 \qquad \textbf{(eq. 4.2e)}$$

$$K = \frac{1}{s^4 N}\sum_{i=1}^{N} (Z_i - m)^4 \qquad \textbf{(eq. 4.2f)}$$

For profiles, equations 4.2 give the Arithmetic Mean (m), Average Roughness (R_a), RMS Roughness (R_q),Variance (s^2), Standard Deviation (s), the Skewness (Sk), and Kurtosis (K). Also, other profile parameters like the curvature, slope, and Gaussian Ratio were calculated using the following equations:

$$Z'(x) = \frac{\partial Z}{\partial x} = \frac{1}{N-1}\sum_{i=1}^{N-1}\frac{Z_{i+1} - Z_i}{\Delta x} \qquad \textbf{(eq. 4.3a)}$$

$$Curv = -Z''(x) = -\frac{\partial^2 Z}{\partial x^2} = \frac{1}{N-2}\sum_{i=2}^{N-1}\frac{2Z_i - Z_{i+1} - Z_{i-1}}{(\Delta x)^2} \qquad \textbf{(eq. 4.3b)}$$

$$GR = \frac{m}{s} = \frac{\frac{1}{N}\sum_{i=1}^{N} Z_i}{\sqrt{\left[\frac{1}{N}\sum_{i=1}^{N}(Z_i - m)^2\right]}} \qquad \textbf{(eq. 4.3c)}$$

Equations 4.3a and 4.3b give the average slope, and average curvature of a profile at line x parallel to the y-axis. Equation 4.3c produces the Gaussian Ratio (GR) of a profile at line x. Recall that, for Gaussian conditions, $GR = \sqrt{\frac{2}{\pi}}$

Also, the surface slope (surface gradient=SG) and the surface curvature (SC) at a given point, were computed in the following way [12]:

$$SG(x,y) = \sqrt{\left[\left(\frac{\partial Z}{\partial x}\right)^2 + \left(\frac{\partial Z}{\partial y}\right)^2\right]} \qquad \textbf{(eq. 4.4a)}$$

$$SC(x,y) = \frac{1}{2}\left[\frac{\partial^2 Z}{\partial x^2} + \frac{\partial^2 Z}{\partial y^2}\right] \qquad \textbf{(eq. 4.4b)}$$

Where, each term of the above surface equations is obtained using the aforementioned profile equations. Besides the Maximum Depth (MD) in a profile, other derived parameters were included in this study, which are defined in section 4.7.

Now, due to the facts that the actual fracture lines are relatively thick, and also that these lines are not straight, a partition of 20 theoretical fracture locations was performed, at each 5% of W_a, see figure 4.3. Since N=600, then each theoretical fracture location will correspond to 600/20=30 real profiles. Referring again to figure 4.3, one could easily visualize this by just imagining that in between every two of the 20 dotted lines, there are 28 actual profiles accounted for. Therefore, for the computation of the aforementioned profile's parameters and moments, average values of 30 profiles were taken.

% Wa	m	RMS	VAR	SD	K	SK	MAX	SLOPE	CURV
0-5	7.94E-06	3.93E-07	3.5E-11	5.46E-06	1.857	0.148	1.96E-05	-3.116E-05	0.0470
5-10	8.46E-06	4.26E-07	4.3E-11	6.12E-06	1.463	-0.109	1.88E-05	-8.937E-06	-0.3738
10-15	9.27E-06	4.54E-07	4.3E-11	6.17E-06	1.738	0.103	2.081E-05	4.8025E-19	-2.231E-14
15-20	9.25E-06	4.50E-07	3.9E-11	5.99E-06	2.167	0.109	2.276E-05	-1.340E-05	-0.19849
20-25	8.87E-06	4.66E-07	5.5E-11	7.16E-06	1.467	0.090	2.111E-05	2.409E-10	-0.1516361
25-30	9.37E-06	5.00E-07	6.6E-11	7.88E-06	1.533	0.173	2.338E-05	-5.449E-19	-2.175E-14
30-35	1.12E-05	5.68E-07	7.2E-11	8.30E-06	1.718	0.111	2.631E-05	2.177E-06	0.052383
35-40	1.02E-05	5.25E-07	6.3E-11	7.80E-06	1.807	0.111	2.551E-05	2.215E-05	0.000122
40-45	1.59E-05	7.60E-07	9.3E-11	9.61E-06	1.945	0.0835	3.175E-05	1.689E-05	0.0002488
45-50	1.88E-05	8.42E-07	7.1E-11	8.47E-06	2.749	-0.352	3.384E-05	1.833E-05	0.110
50-55	1.37E-05	7.18E-07	1.2E-10	1.10E-05	2.056	0.440	3.562E-05	1.344E-18	2.585E-15
55-60	1.241E-05	6.568E-07	1.084E-10	1.023E-05	2.465	0.566	3.679E-05	-9.773E-06	0.1065
60-65	1.273E-05	6.500E-07	9.644E-11	9.572E-06	3.720	0.789	4.080E-05	2.177E-05	-0.20950
65-70	1.216E-05	6.086E-07	7.981E-11	8.630E-06	2.465	0.241	3.267E-05	3.528E-05	0.051369
70-75	1.263E-05	6.228E-07	7.996E-11	8.561E-06	3.353	0.67335	3.596E-05	1.575E-05	-0.10125
75-80	1.045E-05	5.991E-07	1.174E-10	1.028E-05	3.790	1.16877	4.045E-05	1.650E-05	-1.388E-14
80-85	9.067E-06	5.344E-07	1.012E-10	9.455E-06	3.393	1.00584	3.577E-05	2.833E-05	-0.048
85-90	9.118E-06	4.88E-07	6.945E-11	7.758E-06	2.022	0.40932	2.711E-05	3.0785E-05	0.09557
90-95	9.659E-06	4.776E-07	5.1371E-11	6.608E-06	1.516	-0.13047	2.091E-05	2.4346E-05	0.18752
195-00	8.992E-06	4.464E-07	4.666E-11	6.235E-06	1.637	0.11004	2.078E-05	-7.638E-06	-0.0918

Table 4.1: Example Table of Average Parameters computed at every 5% of Wa, for ACL=45 and D=45

This is actually a very accurate approximation since each partition only corresponds to a total length of 0.5”/20=0.025 inches or 635 micrometers. Table 4.1 shows an example of this.

4.3 Effects from Bending Moment, Second Moment of Area

For a center-loaded, simply supported beam, with a rectangular shape, the maximum tensile stress occurs on the outermost point of the convex side at the center of the beam.

$$\sigma = \frac{Mz}{I} \qquad \text{(eq. 4.5)}$$

Where “M” is the bending Moment, “z” is the distance from the neutral axis, and “I” is the Second Moment of Area, or Moment of Inertia. If the cross section was smooth and even, equation 4.5 could easily be evaluated. However, roughness introduces changes in the evaluation of such equation, and the effects of M, z, and I must be investigated and accounted for, if non negligible.

4.3.1 Effects from Bending Moment

Since 3-point bending tests were performed, a linear v-shape curve was convoluted with all parameters to account for maximum bending stress in the center of the shim. This can be easily deduced from the fact that for a center-loaded simply supported beam, the Deflection and Moment equations are given by [13], (refer to figure 2.11):

$$w(x) = -\frac{1}{48}\frac{P}{EI}(3W_a^{\,2} \cdot x - 4x^3) \qquad \textbf{(eq. 4.6a)}$$

$$M(x) = \frac{\partial^2 w}{\partial x^2} EI \qquad \textbf{(eq. 4.6b)}$$

Combining Equations 4.6, leads to the simple and linear relationship [1],

$$M(x)=\begin{cases}\frac{1}{2}Px & 0\le x\le\frac{sl}{2}\\ \frac{1}{2}P(sl-x) & \frac{sl}{2}<x\le sl\end{cases} \qquad \textbf{(eq. 4.7)}$$

Where "P" is the load applied and "sl" is the span length (see table 2.3). Now notice that Normalizing $M(x)/M_{max}$ and accounting for the fact that our length of interest (W_a) is only 1/6 of the span length, a plot similar to that of figure 4.4 is obtained.

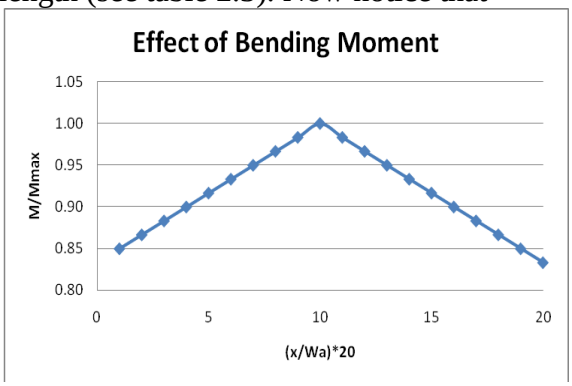

Fig. 4.4- Inverse V-shaped effect of bending moment on stress

4.3.2 Effects of the Second Moment of Area

The Second Moment of Area, or Moment of Inertia, I, with respect to an axis is the sum of the products obtained by multiplying each element of the area dA by the square of its distance from the orthogonal axis, or,

$$I=\int z^2 dA \qquad \textbf{(eq. 4.8)}$$

Since obviously the distance from the neutral axis to the rough surface is changing, I must

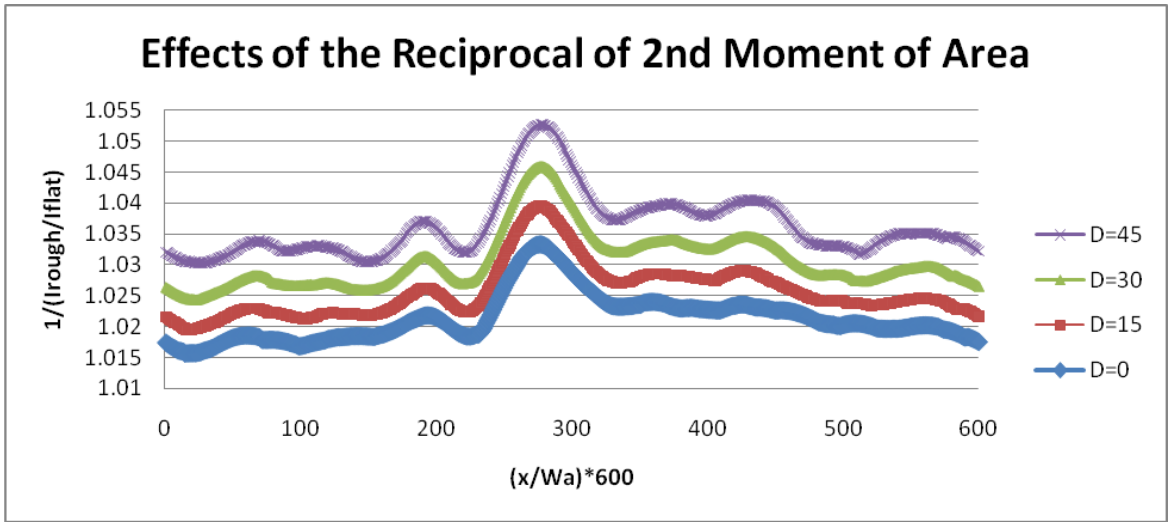

Fig. 4.5- Effect of Reciprocal of Moment of Inertia on Stress for a Random Surface with ACL=45 at various D

be computed numerically at each particular location, see figure 4.3. The effects of I are shown in figure 4.5. Note the ordinate axis in that plot is the reciprocal of the ratio I/I_{flat}, where I_{flat} is the second moment of area of a perfect flat shim. Therefore, "I" has inversely proportional effects on the bending stress by a small yet noticeable value. For ACL=45, the reciprocal of "I" can increase the bending stress by up to the range 3-5%, depending on the depth of the surface (D). However, a combined effect is sought for and discussed starting in the next section.

4.3.3 M, I, z Combined Effects

Mixing the effects of Bending Moment,M, Second Moment of Area, I, and Distance to Neutral Axis, z, a combined effect is obtained. Figure 4.6 shows this for a RR surface with

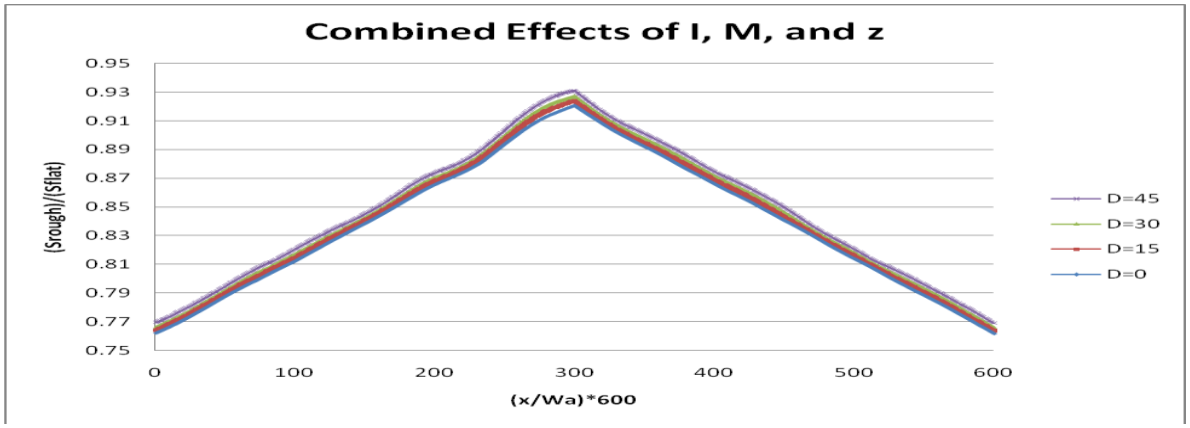

Fig. 4.6- Combined effects on a RR surface with ACL=45

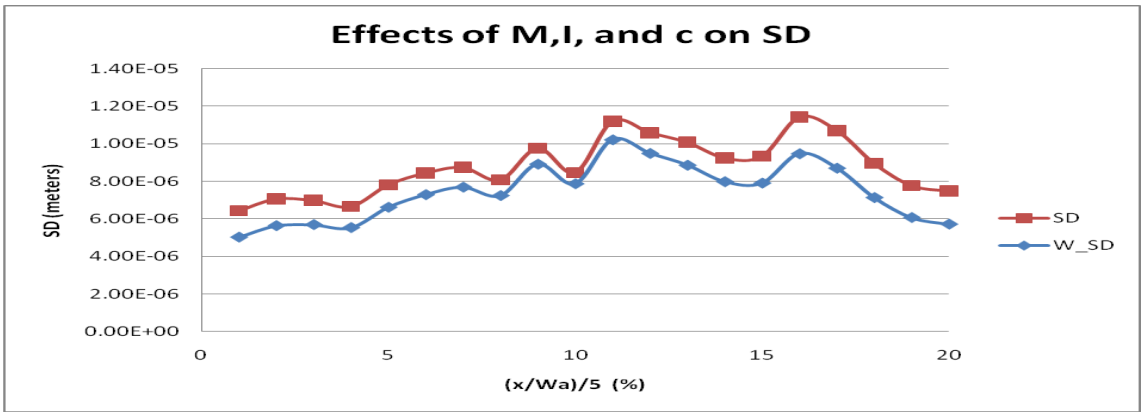

Fig. 4.7- Combined Effects of M, I and z on Standard Deviation of profiles along bending axis, for a RR surface with ACL=45. Notice that c in this plot stands for distance to neutral axis.

ACL=45, at various values of D. Notice that the dominating shape looks like the bending moment aspect of figure 4.4, however the maximum value near the center of the shim does not go to 1, this is due to the inflence of I and z. Applying these combined effects to, for example, the Standard Deviation, of some surface, a plot similar to that of figure 4.7 is obtained. Notice that these shapes are dependent on the RR of the surface but the Moment has the highest influence at this early stage of degradation.

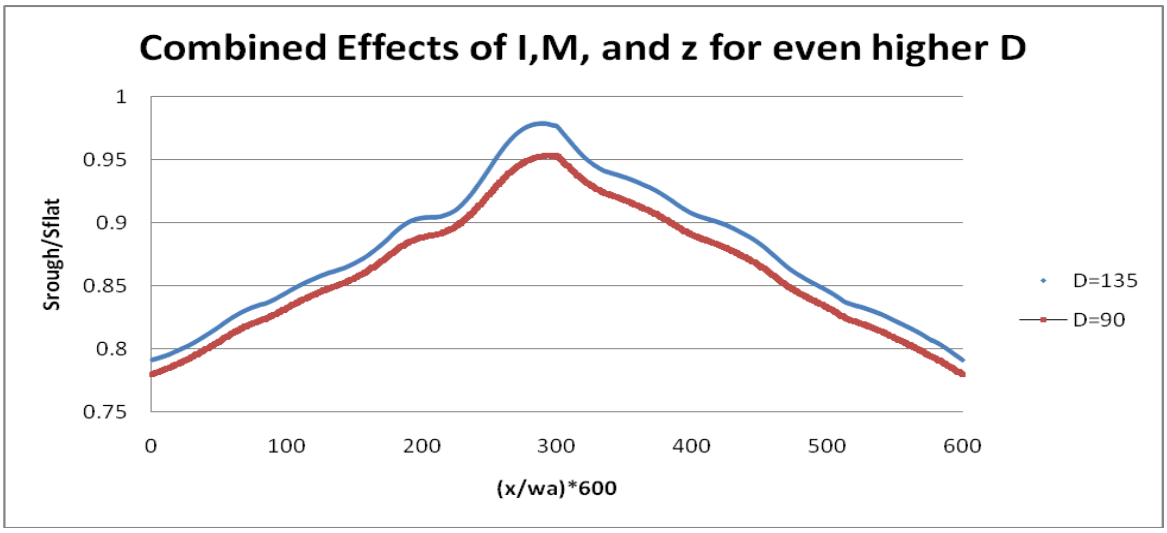

Fig. 4.8- Combined effects on a RR surface with ACL=45, for D=90 and D=135

However, if D is increased by higher amounts, a more uneven effect is seen. For instance, for D=90 and 135, the combined effects seen in figure 4.6 are changed to those shown in figure 4.8. Notice in this case, that the Bending Stress (due to loading only) of a rough surface can reach up to about 98% of that of flat surface, as opposed to the 93% obtained with D=45. This is already saying that as ablation gets deeper, Stress Concentration due mere Bending Moment increases.

These effects affect the value of σ_{load}, in equations 4.1a or 4.1b. So combining all these effects a relationship is proposed for the function $\mathcal{H}$, as follows:

$$\mathcal{H}(x) = \frac{\sigma_{rough}}{\sigma_{flat}} \sum_{i=0}^{n} k_i F_i(x, i) \qquad \textbf{(eq. 4.9)}$$

Where the quotient in the RHS of (4.9) is the ratio of stress (due to bending moment) for a rough surface to that of a perfect flat surface, the rest of the variables and constants are as defined previously. The dependence of F on the parameters defined in equations 4.2, 4.3, and 4.4 is investigated next.

4.4 Stress Concentration at the Interfaces

Looking at the plot of figure 4.2, a rather siginificant value of $\mathcal{H}$ is noticed at both flat-to-rough interfaces. This same trend was observed for medium ACL ($25 \leq ACL \leq 75$, approximately). However, it was observed that for low ACL surfaces, $\mathcal{H}(0)$ and $\mathcal{H}(Wa)$ are not as significant. In General, these effects are due to high stress concentration caused by the irregularities in the flat-to-rough surface interfaces. This lead to the decision of investigating $\mathcal{H}$ away from the ends, approximately between 5%Wa and 95%Wa. This is actually in agreement with St. Venant's Principle (St. Venant 1855) [14]. So from now on in the present study, and unless otherwise specificed, Fracture Location Probability (or Density) Function, $\mathcal{H}/\mathcal{N}$ will be refered to as occuring away from the interfaces.

4.5 Degree of Scatterness

Let S_D be a function such that:

$$S_D = \frac{N_{H1} - 1}{N_{H1} + N_{H0} - 1} \qquad \textbf{(eq. 4.10)}$$

Where N_{H1} is the number of locations at which function $\mathcal{H} \neq 0$ and N_{H0} is the number of locations at which $\mathcal{H}$=0. Then, we call S_D the degree of scatterness of function $\mathcal{H}$. Notice that when fracture takes place at every location, then N_{H0}=0 and therefore S_D=1, and so $\mathcal{H}$ is said to be Completely Scattered. On the other hand, when there is only one location at which $\mathcal{H}$ is nonzero, i.e., fracture is completely localized, then S_D vanishes. So $S_D \in$ [0,1]. It is important to keep in mind, though, that S_D could be misleading in cases where, for example, there are both one highly concentrated location (a location where $\mathcal{H}$ is large) and several enough low concentrated locations (where $\mathcal{H}$'s are very low). This is due to the fact that S_D has been defined in such a way that it does no count for the weight of $\mathcal{H}$ at each location. However, for this particular study, equation 4.10 gives a good estimate of the degree of scatterness (dispersion) of $\mathcal{H}$, since the total number of fractures ($\mathcal{N}$) is not too large.

4.6 Correlation

Function $\mathcal{H}(x_i/w_a)$ for different ACL and D was correlated with the aforesaid moments and parameters defined in equations 4.2 thru 4.4, plus the ones to be discussed in later sections. Bivariate correlations were used to find Pearson's product-moment correlation coefficient. The Pearson Coefficient is a dimensionless index that can measure linear dependence between two variables [15], in order words it is invariant to linear transformations of either compared variable. Pearson initially formulated a mathematical relationship for this rather important measure in 1895, as follows:

$$R = \frac{\sum \left(A_i - \overline{A}\right)\left(B_i - \overline{B}\right)}{\left[\sum \left(A_i - \overline{A}\right)^2 \sum \left(B_i - \overline{B}\right)^2\right]^{\frac{1}{2}}} \qquad \textbf{(eq. 4.11)}$$

Where, A and B are any pair of variables to be compared. It can be proved, using the Cauchy-Swartz inequality that the absolute value of the numerator of equation (4.11) is less than or equal to the denominator which makes R be bounded such that, $R \in [-1,1]$.

Now, examining more closely the best correlation possible that can be obtained with parameters and factors, it is notice that it is precisely the existence of points x_0, such that $\mathcal{H}(x_0) = 0$, what impedes the correlation coefficient from becoming unity. A test of a perfectly correlated set of values was performed. Some of the values of one of two variables compared were substituted with zeros, in order to simulate a case similar to the results of our study. The idea was to explore the different extreme cases and to find the best maximum correlation obtainable. The results show that if all breaks occurs at one location, and this is, in turn, correlated perfectly to some parameter, then the **Rmax=0.767**. Notice that, as it was clarified this Rmax value was calculated for extreme case when there is only one location at which H is nonzero, i.e., when the degree of scatterness, S_D, is zero. Also notice that, as S_D increases Rmax increases. Conclusively, for a perfectly correlated pair of variables, Rmax ranges from 0.767 to 1.0, when S_D goes from 0 to 1. This is very important to properly interpret the results obtained and to be presented in chapter 5.

Now, let $R_{\mathcal{H}m}$ be Pearson's correlation coefficient between parameter "m" and function $\mathcal{H}/\mathcal{N}$. So, for example, the correlation between kurtosis, skewness, and max depth with $\mathcal{H}$ are represented as $R_{\mathcal{H}k}$, $R_{\mathcal{H}Sk}$, $R_{\mathcal{H}MD}$, respectively.

4.7 Derived Parameters

Since the Pearson's correlation shows linear relationship, then other parameters resulting from the combination of the statistical ones must be also investigated. This discussion will start with a parameter proposed by Hinderliter et al. [16]:

$$\frac{Stress_G(t)}{Stress_G(0)} = \left(1 + \frac{kt}{(RMSRoughness(0))^2}\right)^{-\frac{1}{4}} \qquad \textbf{(eq. 4.12)}$$

Where the subscript "G" comes from the fact that equation (4.12) was derived from Griffith's criterion formula. "kt" can be interpreted as the surface RMS roughness at any time t, based on the Central Limit Theorem evolution of the surface. The ratio (4.12) is then directly proportional to the toughness of the polymeric coating. Its reciprocal then will be directly proportional to the Fracture Density, $\mathcal{H}/\mathcal{N}$. Since for some real cases (like the present study) the Average Surface correlates better than the RMS, then it is proposed here to use a parameter similar to the reciprocal of (4.12) but based on the Average Roughness (AR). Both of these parameters are referred to, in this study, as the RMS HM-factor and the AVG HM-factor.

Another parameter is proposed here based on the results developed by Inglis [17]. The first quantitative evidence for the stress concentration effect of flaws was provided by Inglis, who analyzed elliptical holes in flat plates [18]. His analyses included an elliptical hole 2a long by 2b wide with

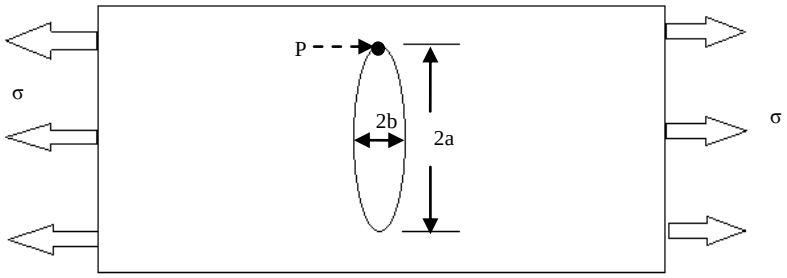

Fig. 4.9- Elliptical Hole in flat plate

applied stress perpendicular to the major axis of the ellipse (see figure 4.9). The stress at the tip of the major axis (point P) is given by:

$$\sigma_P = \sigma\left(1+\frac{2a}{b}\right) \qquad \textbf{(eq. 4.13)}$$

So the Stress Concentration Factor, in this case, is given by,

$$k_t = \left(1+\frac{2a}{b}\right) \qquad \textbf{(eq. 4.14)}$$

If the elliptical hole of figure 4.9 is cut in half parallel to the minor axis, a notch of depth "a" is obtained. Now extending this idea to a multi-crack arrangement, an array of cracks of a_i depth is obtained (figure 4.10). *It is proposed here* an average Stress Concentration Factor, defined as follows,

$$k_t = \left[1+2\frac{AR}{ACL}\right] \qquad \textbf{(eq. 4.15)}$$

Where AR=Average Roughness and ACL is Auto Correlation Length. Despite the fact, that half the pit depth is being used, the factor 2 is kept based on the approximation also proposed by Inglis for a notch that is not elliptical except at the tip. In the results, the Stress Concentration Factor given by equation 4.15 is referred to as "Modified Inglis Factor". Of course, secondary effects due to the presence of several pits close to each other are yet to be considered in the proposed formula (4.15);

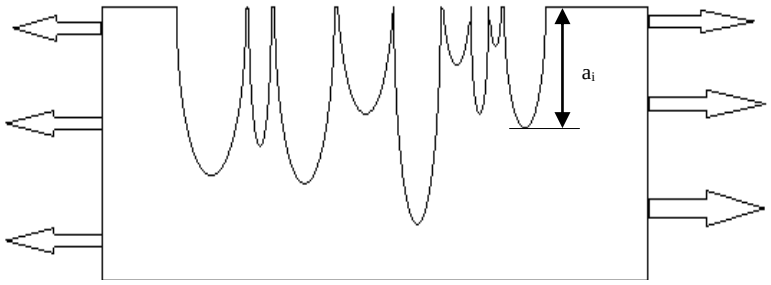

Fig. 4.10- Superposition of several half elliptical holes

notwithstanding, this is just an initial approximation. Besides the secondary effects due to the superposition of pits is essentially the purpose of this study.

4.8 Finite Element Analysis

Surfaces developed in Matlab® were imported into COMSOL® to observe the stress distribution via FEA. An interpolation function was used to interpret the surfaces as seen in figure 4.11. This surface was then digitally "imprinted" on a block as shown in figure 4.12. Notice that since the damage is so small the roughness is barely seen. Also, notice that a cylindrical beam was included to simulate the actual ASTM's D790 3-Point bending test that was used in the present study. Also, another approach was used that involved tensile loading on a thinner film, instead of the whole thickness. Normal and fine mesh were used. A sample of a normal mesh on the ablated area is shown in figure 4.13. A Linear Elastic Material physics under the Solid

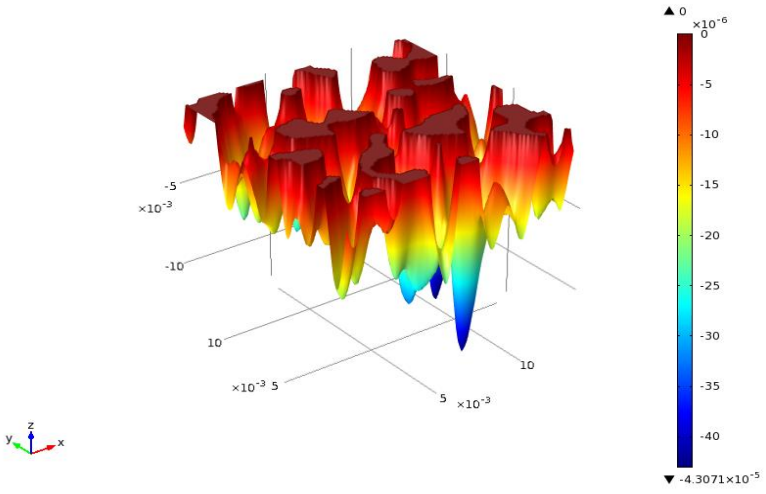

Fig. 4.11- Surface plot in COMSOL®

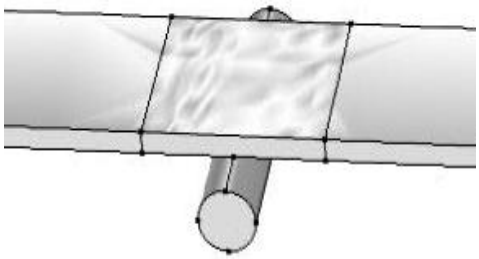

Fig. 4.12- one of the two models simulated

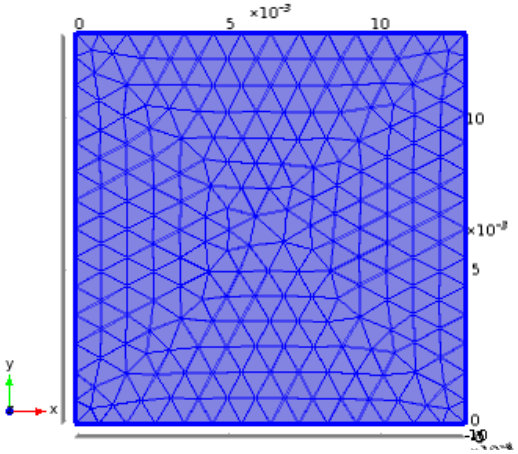

Fig. 4.13- Normal size mesh used

Mechanics module was used. For one case boundary tensile loads were used parallel to the x-axis. For another case, boundary loads were located as to produce a bending moment on the beam, see figure 4.13.

At this stage of this ongoing research, the FEA output obtained was only used to compare the experimental and statistical analysis.

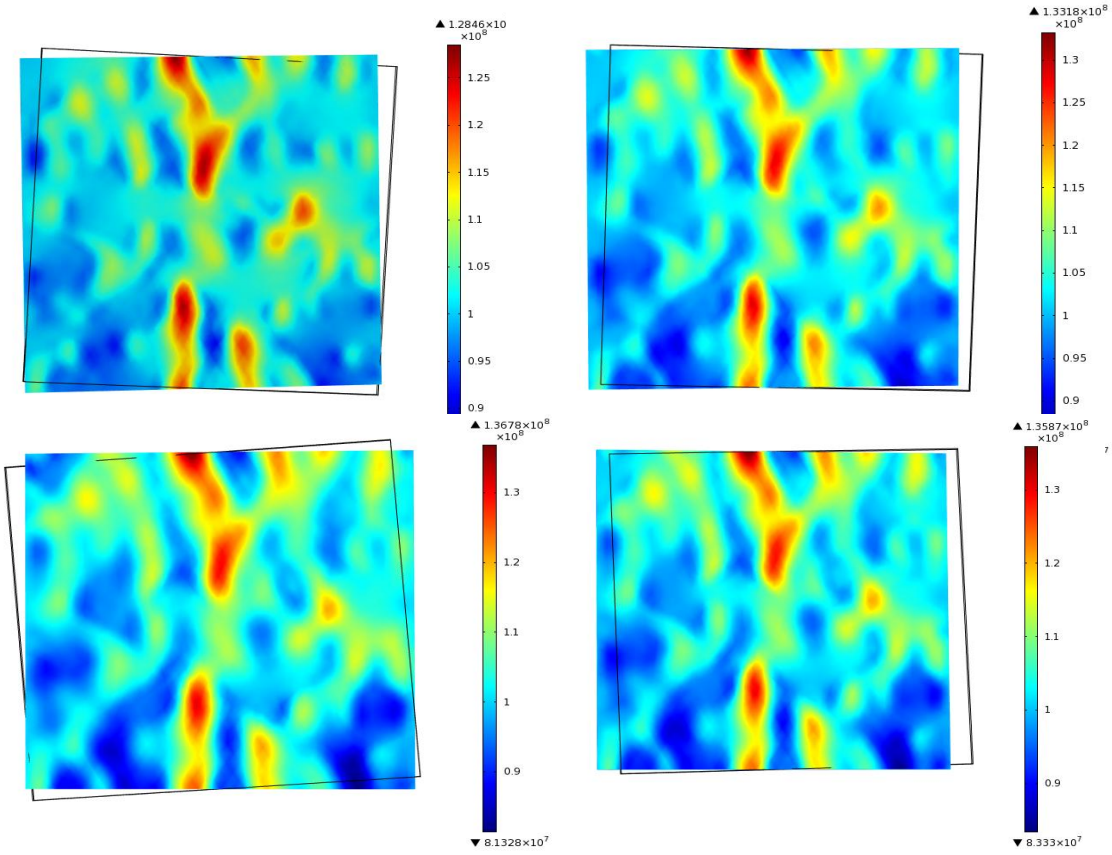

Fig. 4.14- Von Mises (octahedral) stress distribution (Pascals) for ACL=45, D was varied as: top left, D=0; top right, D=15; bottom left, D=30; bottom right, D=45. Surface deformation and displacement field of material included.

Figure 4.14 shows octahedral stress distribution for ACL=45, and D=0, 15, 30, and 45. Notice in those plots the following:

- The interfaces high concentration stresses were removed due to the type of model.
- The scale of the octahedral stresses (in units of Pascal) changes for each plot.
- High stress concentration´s degree of dispersion decreases as D increases, which is very much agreeable with what was observed experimentally.
- The locations of high stress concentration agree with the locations found experimentally.

CHAPTER 5 Results and Discussion

5.1 Results

5.1.1 Descriptive Statistics

Table 5.1 presents a sample of the Descriptive Statistics used in developing the results. Table 5.2 shows tabulation, for a particular Auto Correlation Length, and at several D, of the Pearson's moment-product coefficient for the following profile parameters: Average, Root Mean Squared, Standard Deviation, Kurtosis, Skewness, Maximum Depth, Slope, Curvature, and the derived parameters. In that table it is included the Sig.(2-tailed) value, the Sum of Squares and Cross-products, the Covariance, and the number of scores. Even though they are not shown in those tables, Gaussian Ratio is also included among the parameters considered. In Table 5.2, D varies from 0 to 135.

Descriptive Statistics

	Mean	Std. Deviation	N
FRACTURE DENSITY	.051	.071	18
Ratio AVERAGE	.894	.372	18
AR HM-factor	1.163	.108	18
Griffith	1.645	.327	18
MOD. INGLIS(EEFECTS)	1.034	.117	18
Ratio RMS	.035	.011	18
RMS H-factor	1.000	0.000	18
RMS HM-Factor	1.017	.006	18
Ratio SD	.812	.243	18
Ratio Kurt	1.117	.488	18
Ratio Sk	-.600	.266	18
Ratio MAX	.510	.178	18
SLOPE	0.00	0.00	18
CURV	-.018	.059	18
Gaussian Ratio	.730	.179	18

Table 5.1: Descriptive Statistics sample table.

		Ratio AVERAGE	AR HM-factor	Griffith	MOD. INGLIS(EEFECTS)	Ratio RMS	RMS HM-Factor	Ratio SD	Ratio Kurt	Ratio Sk	Ratio MAX	SLOPE	CURV	Gaussian Ratio
d_H	Pearson Correlation	-.046	-.051	-.031	-.114	.026	.026	.095	.211	-.178	.166	.030	-.152	-.156
	Sig. (2-tailed)	.857	.842	.904	.652	.918	.917	.708	.400	.479	.510	.906	.547	.536
	N	18	18	18	18	18	18	18	18	18	18	18	18	18
d_H	Pearson Correlation	.239	.237	.246	.244	.232	.232	.195	.269	-.128	.300	.043	-.243	.152
	Sig. (2-tailed)	.339	.344	.325	.329	.354	.354	.439	.280	.613	.227	.865	.330	.547
	N	18	18	18	18	18	18	18	18	18	18	18	18	18
d_H	Pearson Correlation	.737**	.746**	.712**	.723**	.593**	.592**	.133	-.076	.507*	.127	.150	.215	.833**
	Sig. (2-tailed)	.000	.000	.001	.001	.010	.010	.599	.764	.032	.617	.552	.391	.000
	N	18	18	18	18	18	18	18	18	18	18	18	18	18
d_H	Pearson Correlation	.767**	.775**	.751**	.751**	.695**	.694**	.275	.039	.335	.239	.071	.081	.664**
	Sig. (2-tailed)	.000	.000	.000	.000	.001	.001	.269	.877	.174	.339	.779	.748	.003
	N	18	18	18	18	18	18	18	18	18	18	18	18	18
d_H	Pearson Correlation	.705**	.713**	.688**	.687**	.633**	.632**	.237	.036	.330	.199	.170	.107	.622**
	Sig. (2-tailed)	.001	.001	.002	.002	.005	.005	.344	.888	.181	.428	.500	.672	.006
	N	18	18	18	18	18	18	18	18	18	18	18	18	18
d_H	Pearson Correlation	.705**	.713**	.689**	.694**	.636**	.635**	.248	.042	.330	.208	.173	.108	.624**
	Sig. (2-tailed)	.001	.001	.002	.001	.005	.005	.321	.867	.180	.408	.494	.670	.006
	N	18	18	18	18	18	18	18	18	18	18	18	18	18

**. Correlation is significant at the 0.01 level (2-tailed).*. Correlation is significant at the 0.05 level (2-tailed).

Table 5.2 Sample output of some of the statistical Parameters for ACL=45, varying D from 0 to 135

5.1.3 Scatter Plots and Correlation

Following is a series 78 scatter plots selected to show the sensitivity of certain parameters at certain ACL and D. Here are shown only for ACL=45, varying D from 0 to 135. Similar data was obtained for other ACL's (see appendix C). The profile parameters shown in these simple scatter plots are Average Roughness, Root Mean Squared Roughness, AR-factor, RMS factor, Griffith factor, Modified Inglis Factor, Maximum (average) Depth, Standard Deviation, Kurtosis, Skewness, Slope, Curvature, and Gaussian Ratio. The y-axis in all plots corresponds to the fracture density $\mathcal{H}/\mathcal{N}$. Other Parameters included are Griffith Factor, Average Roughness HM-factor, RMS Roughness HM-factor and the Modified Inglis Factor. There are 13 plots at each value of D. These plots are shown so that the sensitivity of the Fracture Density (probability) with these parameters and factors can be appreciated. Notice that for D=0 (first 13 plots), the data is completely scatter and it does not show any correlation whatsoever. For D=15, data are still scatter, but not as much as for D=0. For D=30 some trend starts to show for some of the parameter. This trend is actually more appreciated when D=30 is compared with D=45. For the latter, not only the same trend continues but it also grows. This same trend is kept as the surface degrades even deeper (D=90 and D=135), for some of the parameters and factors, especially for those involving either Average Roughness or Root Mean Squared Roughness. A plot using data similar to that shown in table 5.2 confirms this trend, as it depicted in figure 5.2 (after the scatter plots). Some Uncorrelated parameters are included in Figure 5.3 to show the contrast.

Fig. 5.1- Scatter Plots of Fracture Density Vs parameters for ACL=45 D=0

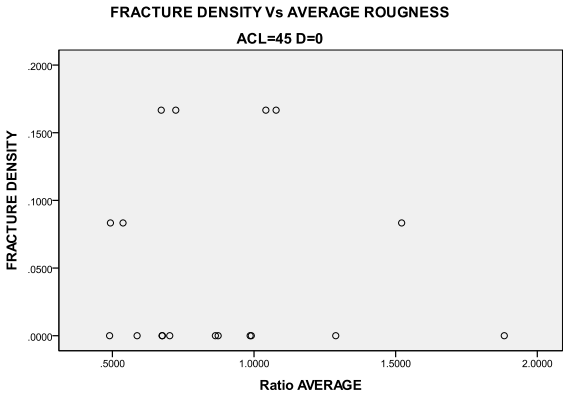

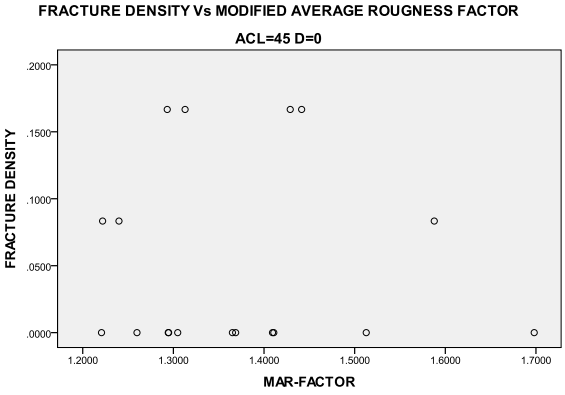

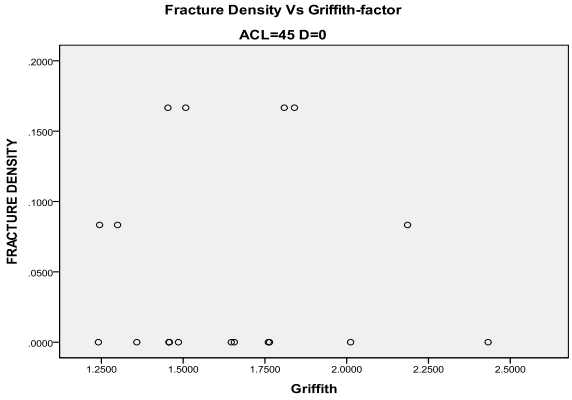

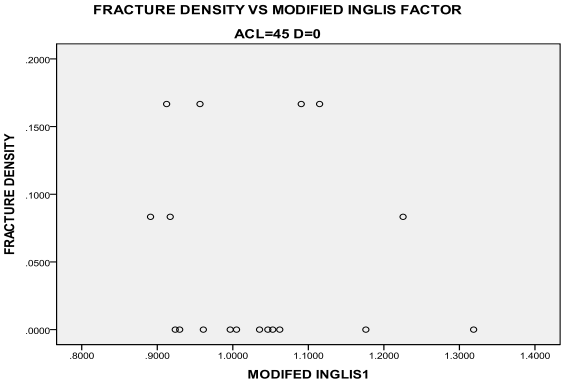

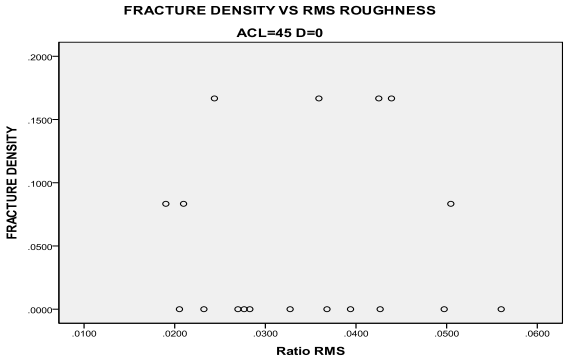

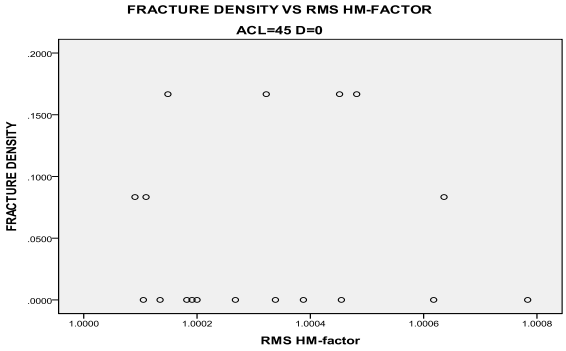

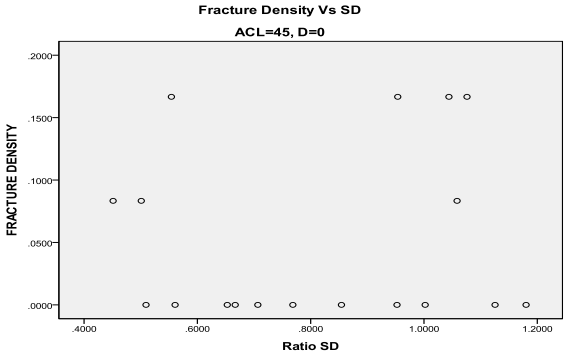

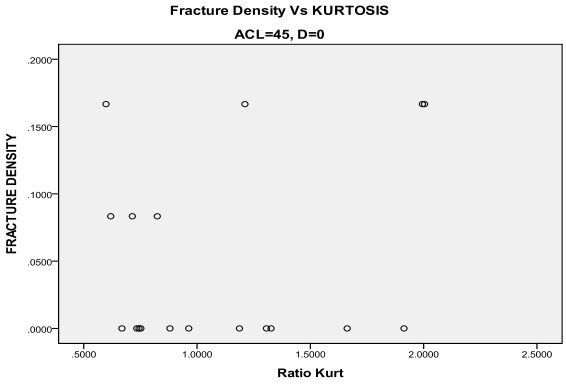

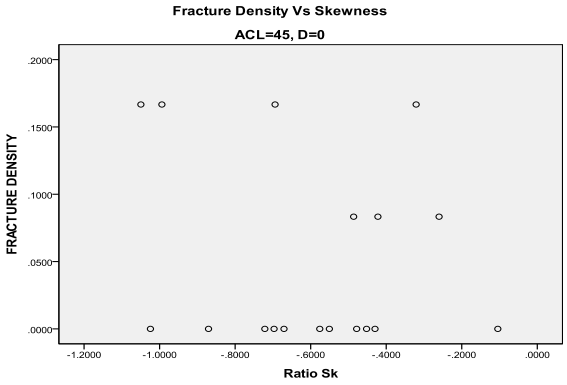
Fracture Density Vs Skewness
ACL=45, D=0
FRACTURE DENSITY
.2000
.1500
.1000
.0500
.0000
-1.2000
-1.0000
-.8000
-.6000
-.4000
-.2000
.0000
Ratio Sk

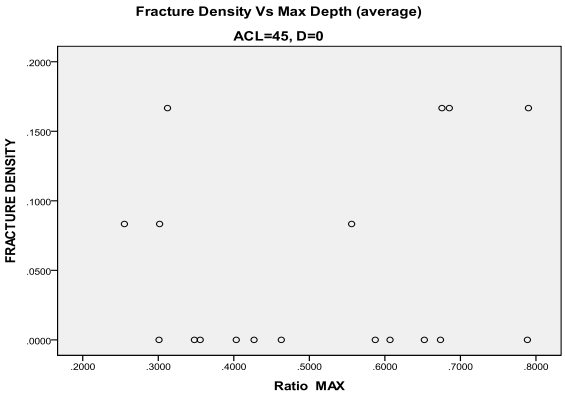
Fracture Density Vs Max Depth (average)
ACL=45, D=0
FRACTURE DENSITY
.2000
.1500
.1000
.0500
.0000
.2000
.3000
.4000
.5000
.6000
.7000
.8000
Ratio MAX

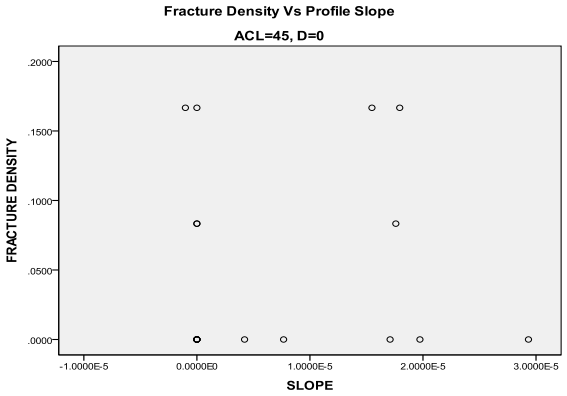
Fracture Density Vs Profile Slope
ACL=45, D=0
FRACTURE DENSITY
.2000
.1500
.1000
.0500
.0000
-1.0000E-5
0.0000E0
1.0000E-5
2.0000E-5
3.0000E-5
SLOPE

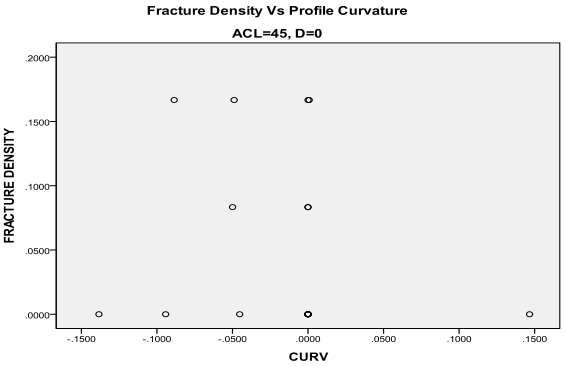
Fracture Density Vs Profile Curvature
ACL=45, D=0
FRACTURE DENSITY
.2000
.1500
.1000
.0500
.0000
-.1500
-.1000
-.0500
.0000
.0500
.1000
.1500
CURV

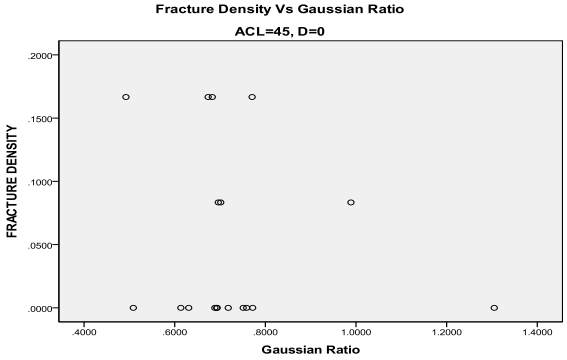
Fracture Density Vs Gaussian Ratio
ACL=45, D=0
FRACTURE DENSITY
.2000
.1500
.1000
.0500
.0000
.4000
.6000
.8000
1.0000
1.2000
1.4000
Gaussian Ratio

Fig. 5.2- Scatter Plots of Fracture Density Vs parameters for ACL=45 D=15

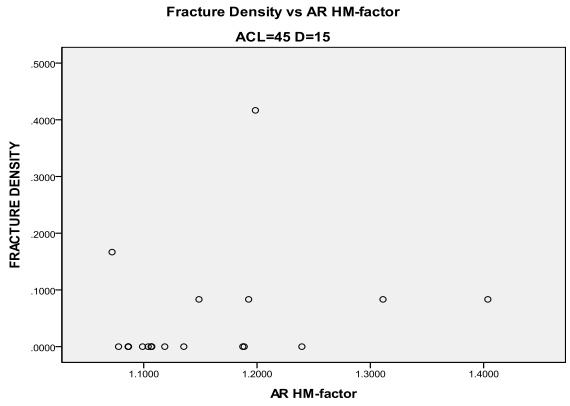

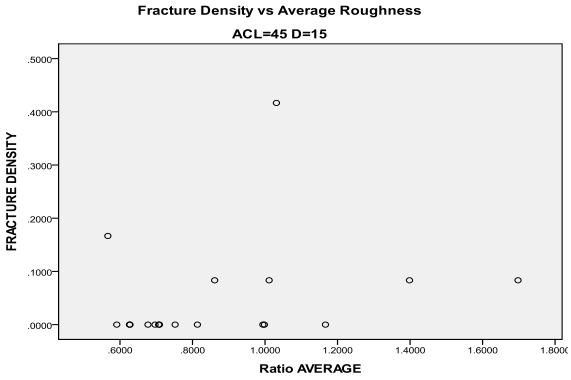

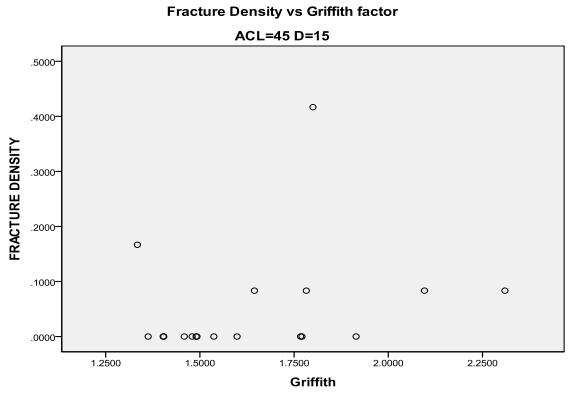

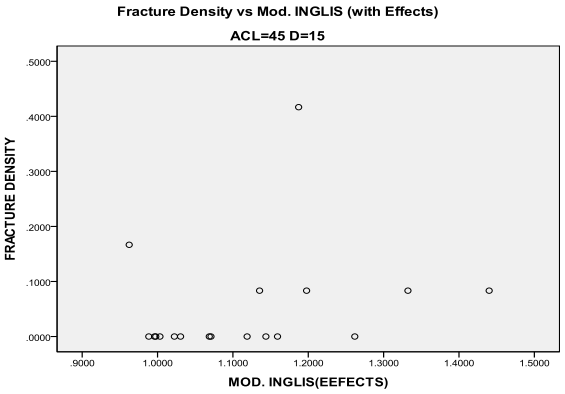

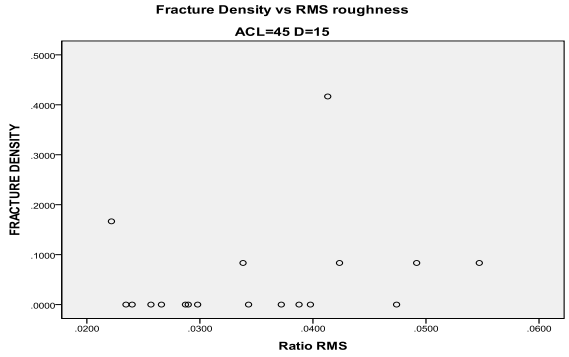

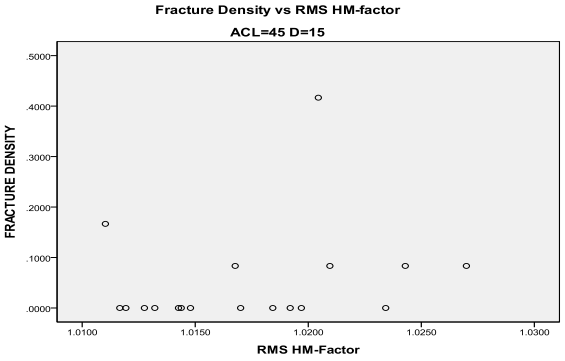

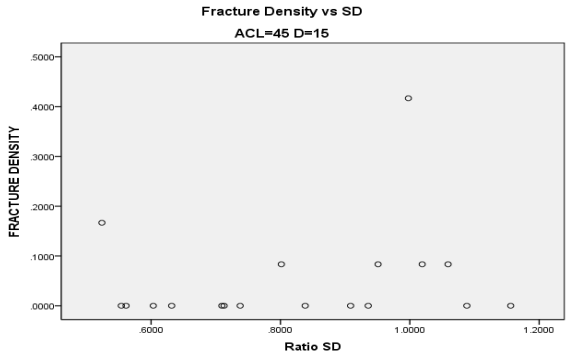

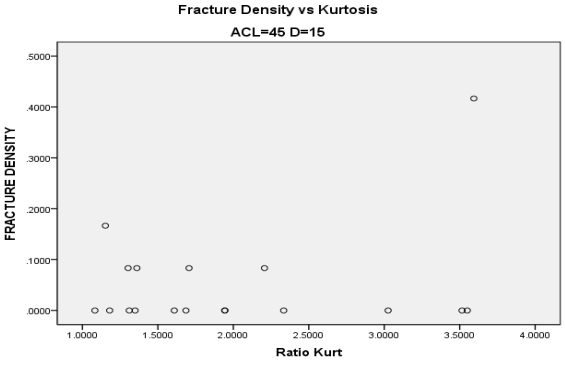

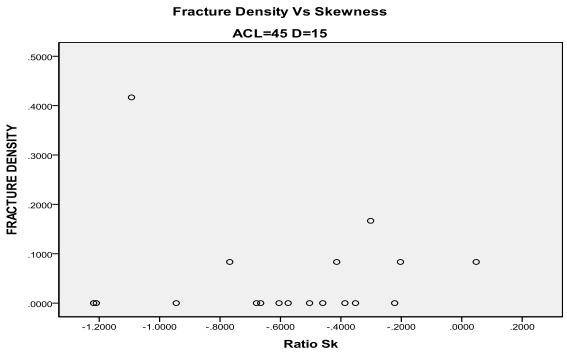
Fracture Density Vs Skewness
ACL=45 D=15
FRACTURE DENSITY
.5000
.4000
.3000
.2000
.1000
.0000
-1.2000
-1.0000
-.8000
-.6000
-.4000
-.2000
.0000
.2000
Ratio Sk

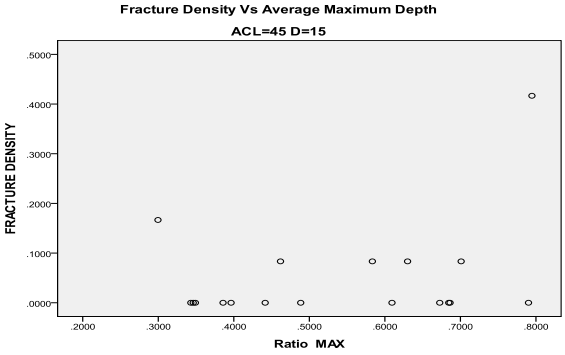
Fracture Density Vs Average Maximum Depth
ACL=45 D=15
FRACTURE DENSITY
.5000
.4000
.3000
.2000
.1000
.0000
.2000
.3000
.4000
.5000
.6000
.7000
.8000
Ratio MAX

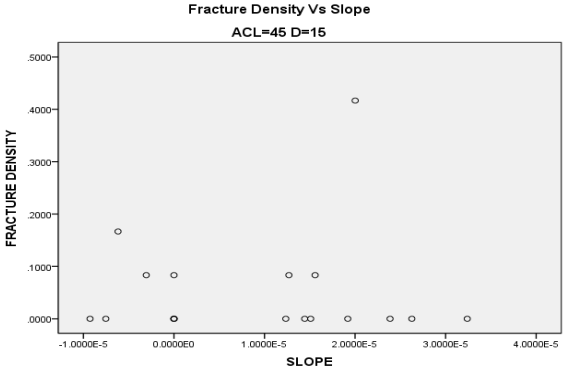
Fracture Density Vs Slope
ACL=45 D=15
FRACTURE DENSITY
.5000
.4000
.3000
.2000
.1000
.0000
-1.0000E-5
0.0000E0
1.0000E-5
2.0000E-5
3.0000E-5
4.0000E-5
SLOPE

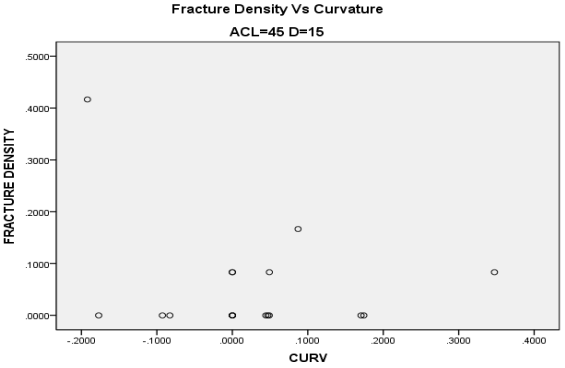
Fracture Density Vs Curvature
ACL=45 D=15
FRACTURE DENSITY
.5000
.4000
.3000
.2000
.1000
.0000
-.2000
-.1000
.0000
.1000
.2000
.3000
.4000
CURV

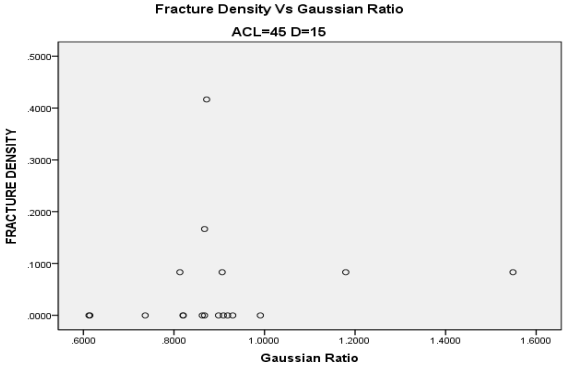
Fracture Density Vs Gaussian Ratio
ACL=45 D=15
FRACTURE DENSITY
.5000
.4000
.3000
.2000
.1000
.0000
.6000
.8000
1.0000
1.2000
1.4000
1.6000
Gaussian Ratio

Fig. 5.3- Scatter Plots of Fracture Density Vs parameters for ACL=45 D=30

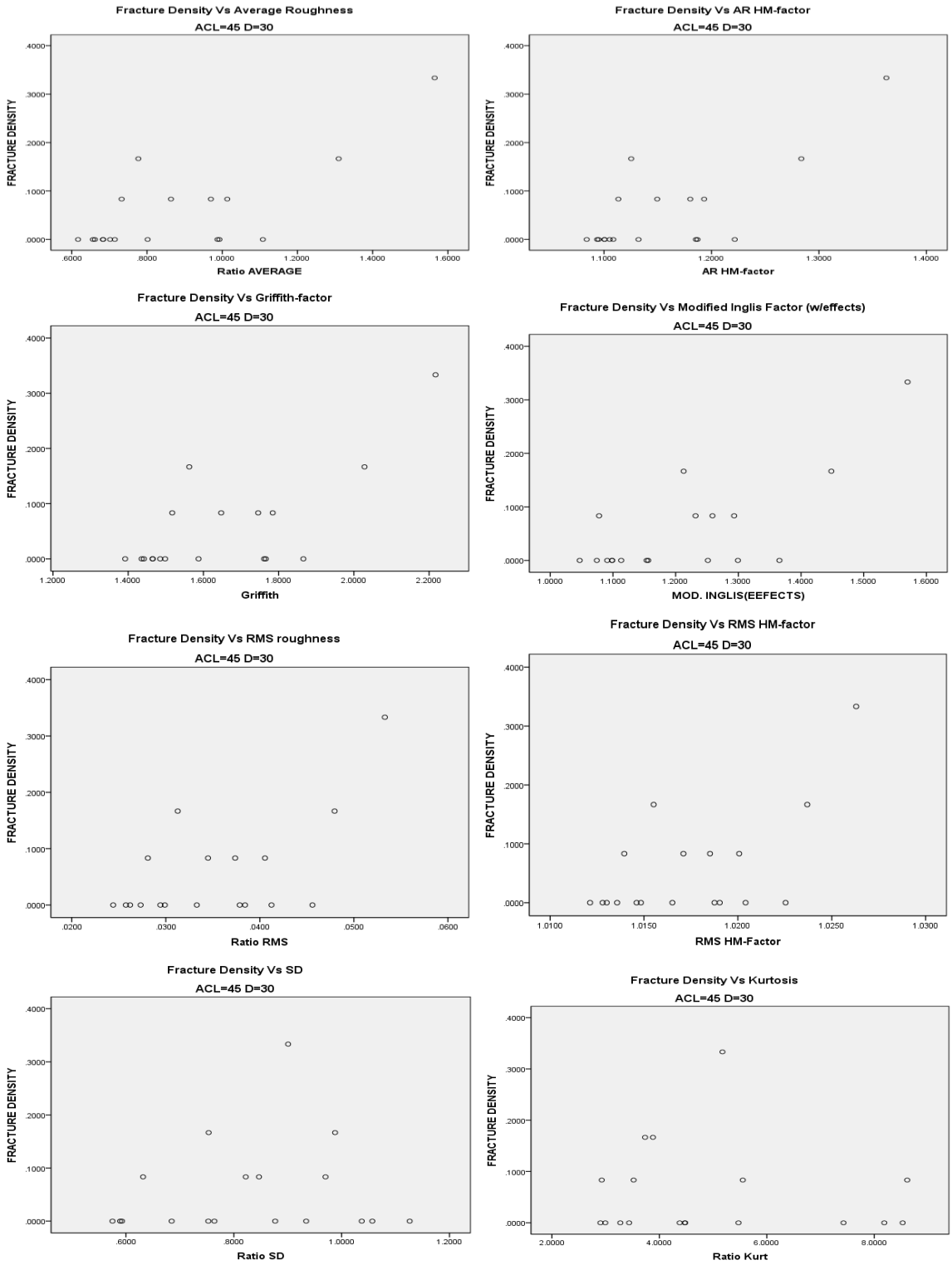

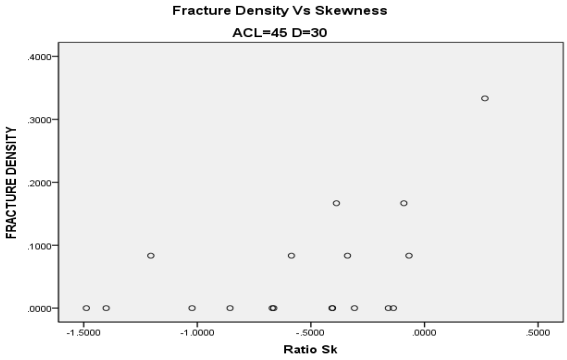
Fracture Density Vs Skewness
ACL=45 D=30
FRACTURE DENSITY
.4000
.3000
.2000
.1000
.0000
-1.5000
-1.0000
-.5000
.0000
.5000
Ratio Sk

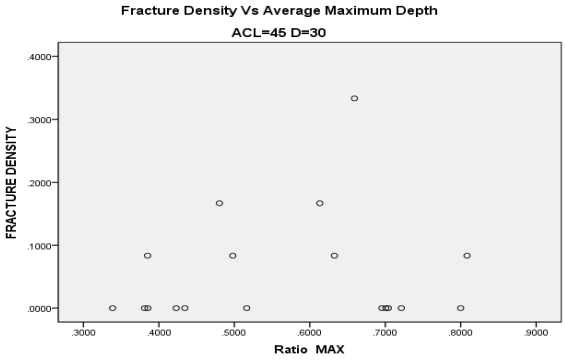
Fracture Density Vs Average Maximum Depth
ACL=45 D=30
FRACTURE DENSITY
.4000
.3000
.2000
.1000
.0000
.3000
.4000
.5000
.6000
.7000
.8000
.9000
Ratio MAX

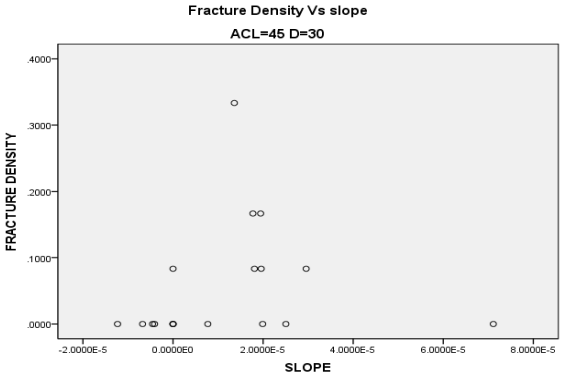
Fracture Density Vs slope
ACL=45 D=30
FRACTURE DENSITY
.4000
.3000
.2000
.1000
.0000
-2.0000E-5
0.0000E0
2.0000E-5
4.0000E-5
6.0000E-5
8.0000E-5
SLOPE

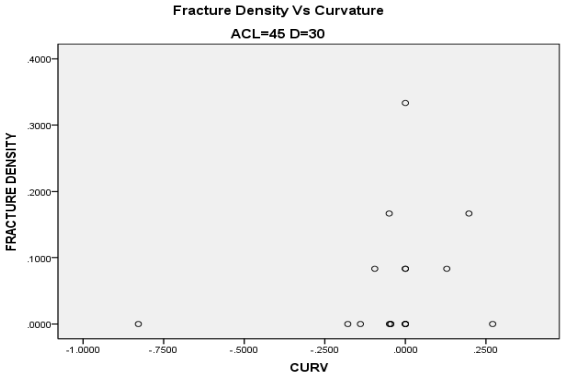
Fracture Density Vs Curvature
ACL=45 D=30
FRACTURE DENSITY
.4000
.3000
.2000
.1000
.0000
-1.0000
-.7500
-.5000
-.2500
.0000
.2500
CURV

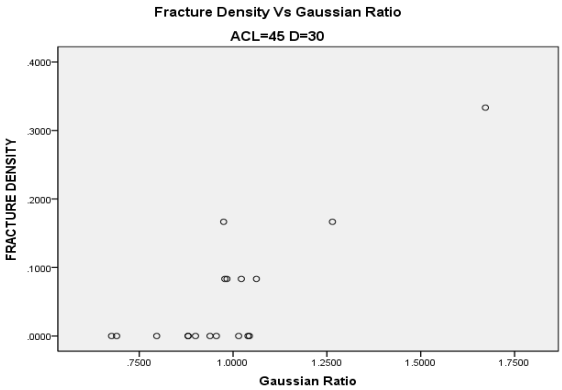
Fracture Density Vs Gaussian Ratio
ACL=45 D=30
FRACTURE DENSITY
.4000
.3000
.2000
.1000
.0000
.7500
1.0000
1.2500
1.5000
1.7500
Gaussian Ratio

Fig. 5.4- Scatter Plots of Fracture Density Vs parameters for ACL=45 D=45

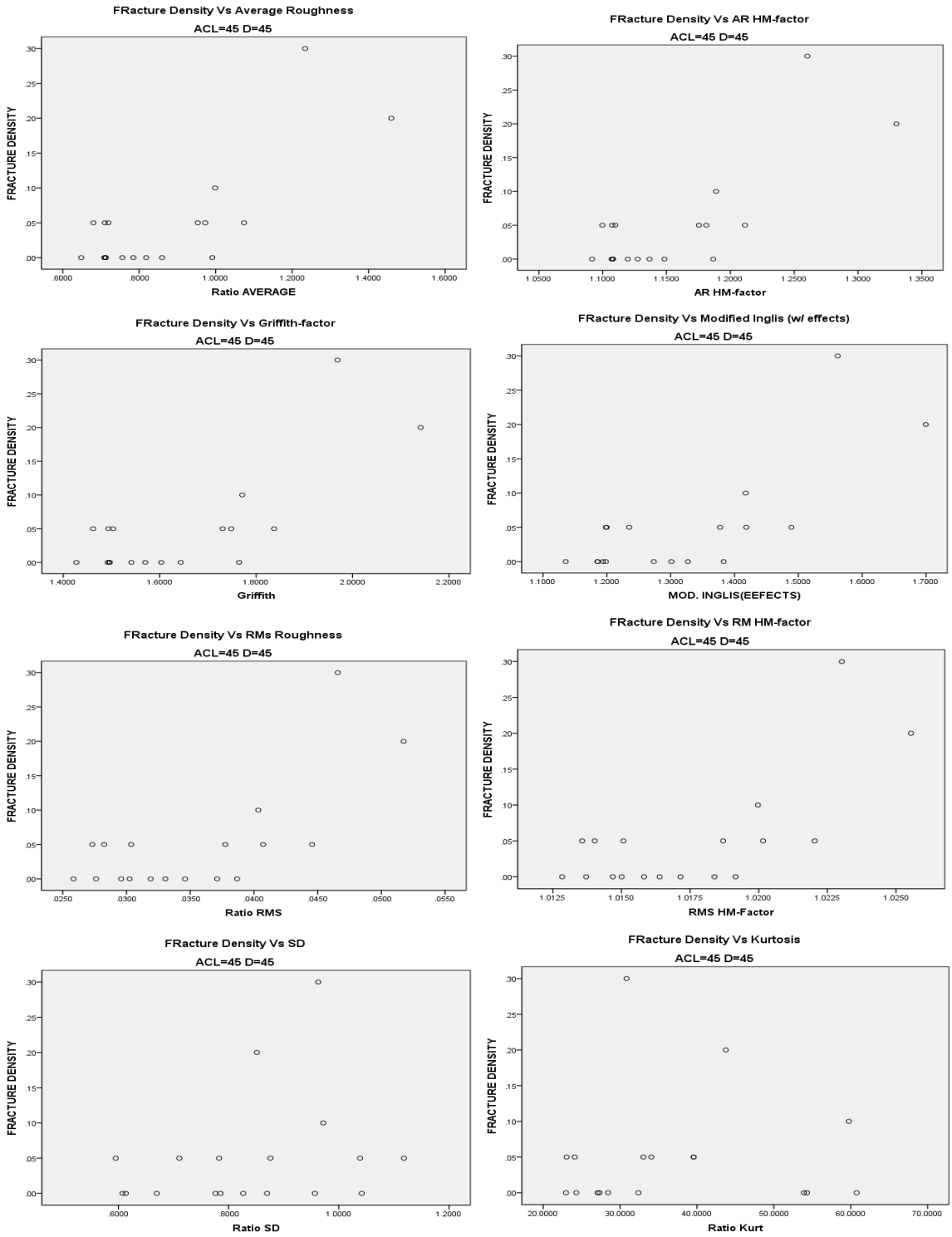

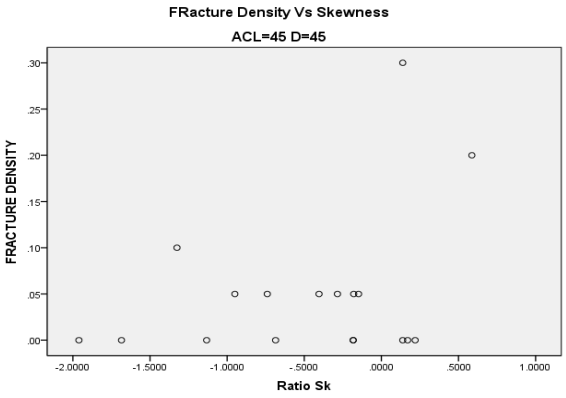
FRacture Density Vs Skewness
ACL=45 D=45
FRACTURE DENSITY
Ratio Sk

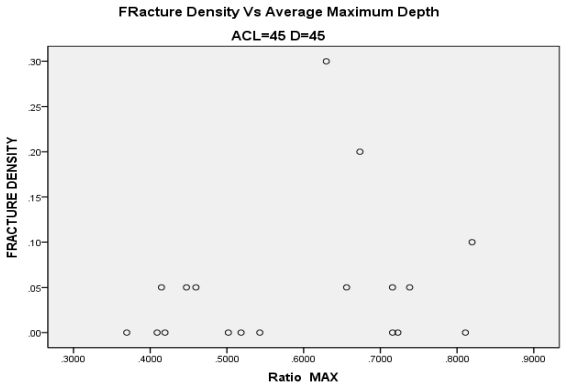
FRacture Density Vs Average Maximum Depth
ACL=45 D=45
FRACTURE DENSITY
Ratio MAX

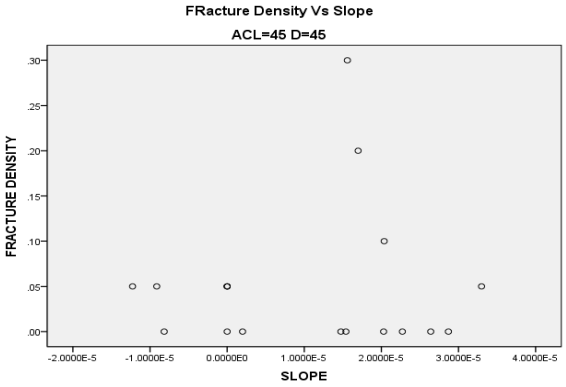
FRacture Density Vs Slope
ACL=45 D=45
FRACTURE DENSITY
SLOPE

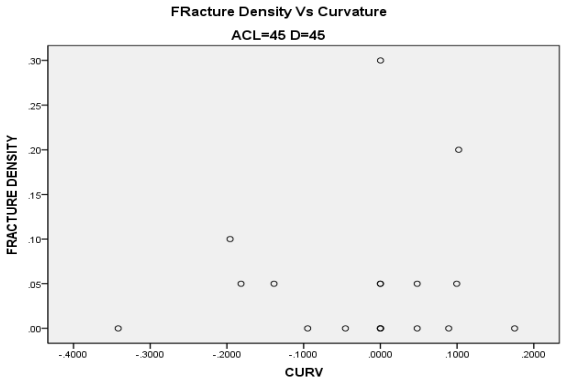
FRacture Density Vs Curvature
ACL=45 D=45
FRACTURE DENSITY
CURV

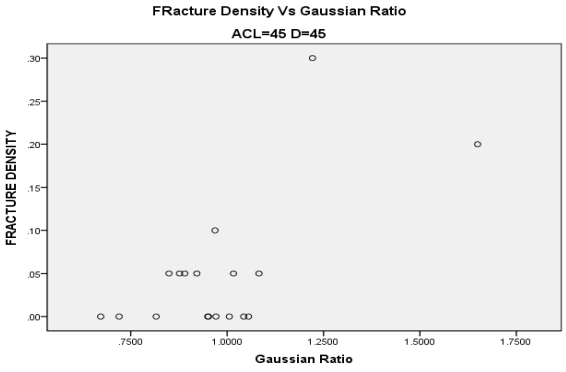
FRacture Density Vs Gaussian Ratio
ACL=45 D=45
FRACTURE DENSITY
Gaussian Ratio

Fig. 5.5- Scatter Plots of Fracture Density Vs parameters for ACL=45 D=90

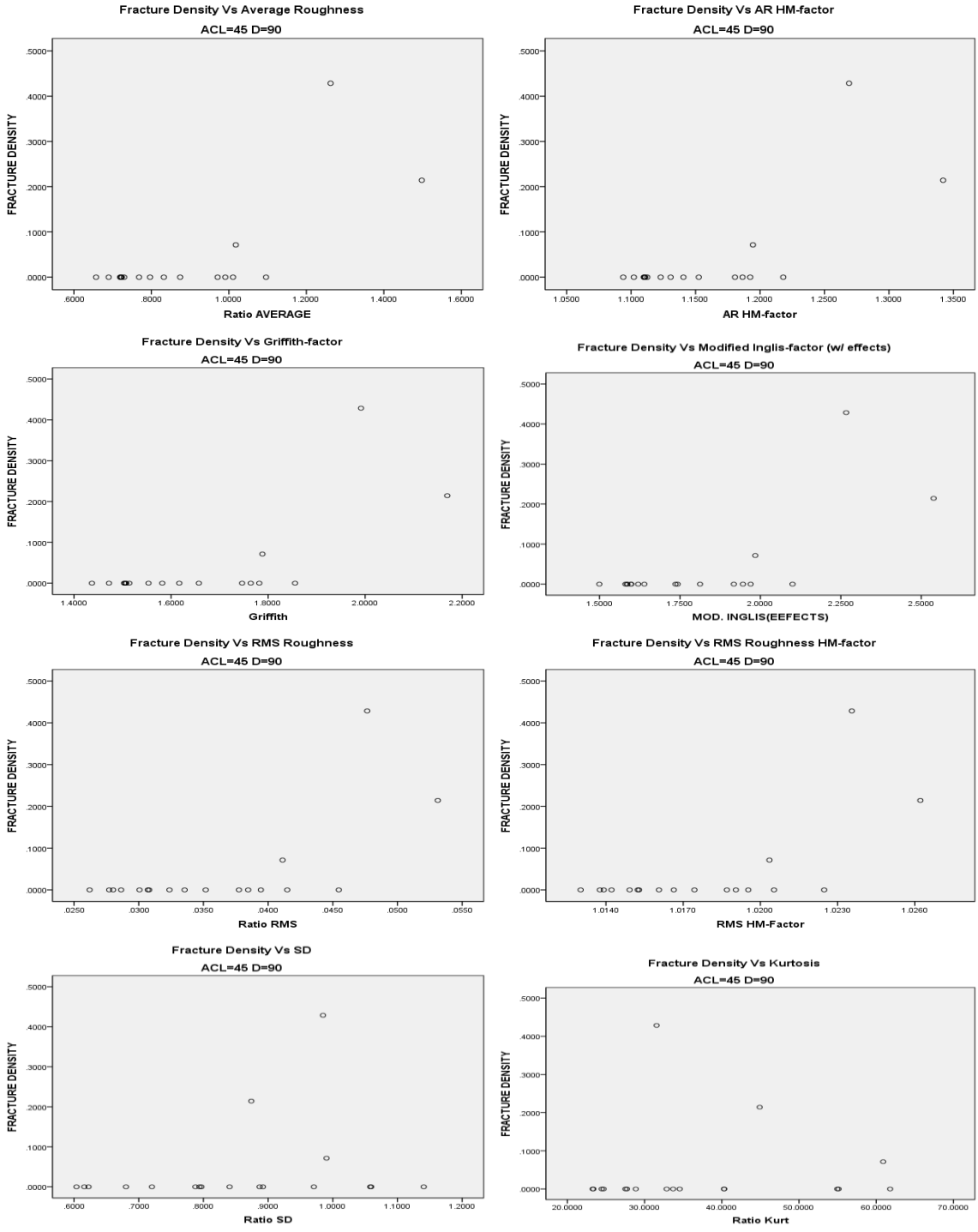

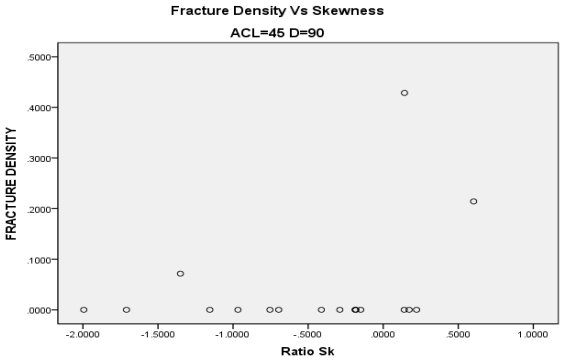
Fracture Density Vs Skewness
ACL=45 D=90
FRACTURE DENSITY
.5000
.4000
.3000
.2000
.1000
.0000
-2.0000
-1.5000
-1.0000
-.5000
.0000
.5000
1.0000
Ratio Sk

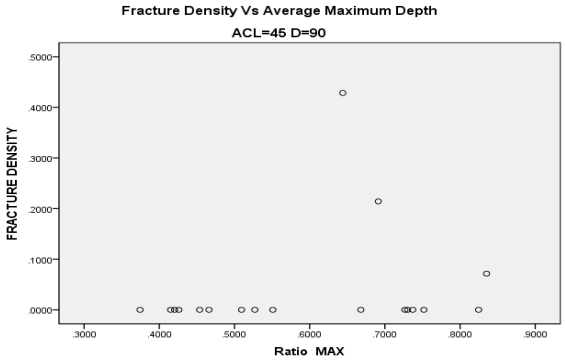
Fracture Density Vs Average Maximum Depth
ACL=45 D=90
FRACTURE DENSITY
.5000
.4000
.3000
.2000
.1000
.0000
.3000
.4000
.5000
.6000
.7000
.8000
.9000
Ratio MAX

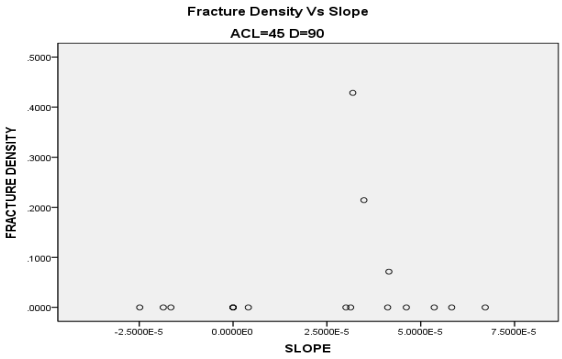
Fracture Density Vs Slope
ACL=45 D=90
FRACTURE DENSITY
.5000
.4000
.3000
.2000
.1000
.0000
-2.5000E-5
0.0000E0
2.5000E-5
5.0000E-5
7.5000E-5
SLOPE

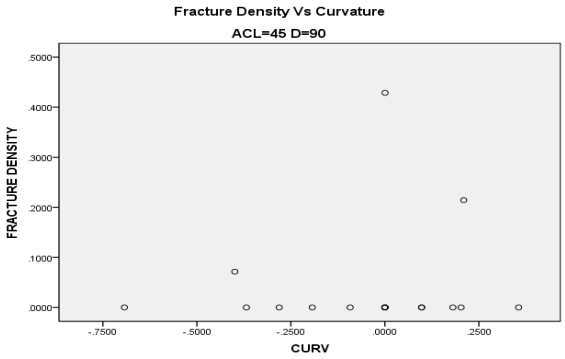
Fracture Density Vs Curvature
ACL=45 D=90
FRACTURE DENSITY
.5000
.4000
.3000
.2000
.1000
.0000
-.7500
-.5000
-.2500
.0000
.2500
CURV

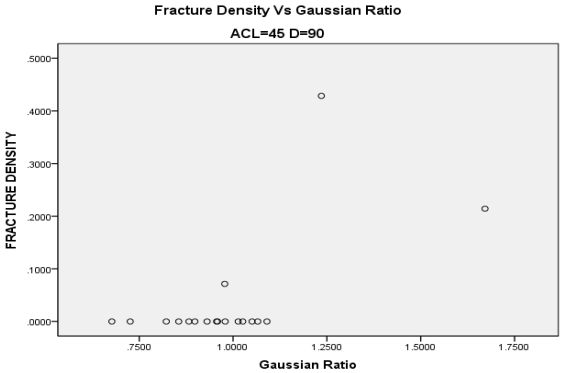
Fracture Density Vs Gaussian Ratio
ACL=45 D=90
FRACTURE DENSITY
.5000
.4000
.3000
.2000
.1000
.0000
.7500
1.0000
1.2500
1.5000
1.7500
Gaussian Ratio

Fig. 5.6- Scatter Plots of Fracture Density Vs parameters for ACL=45 D=135

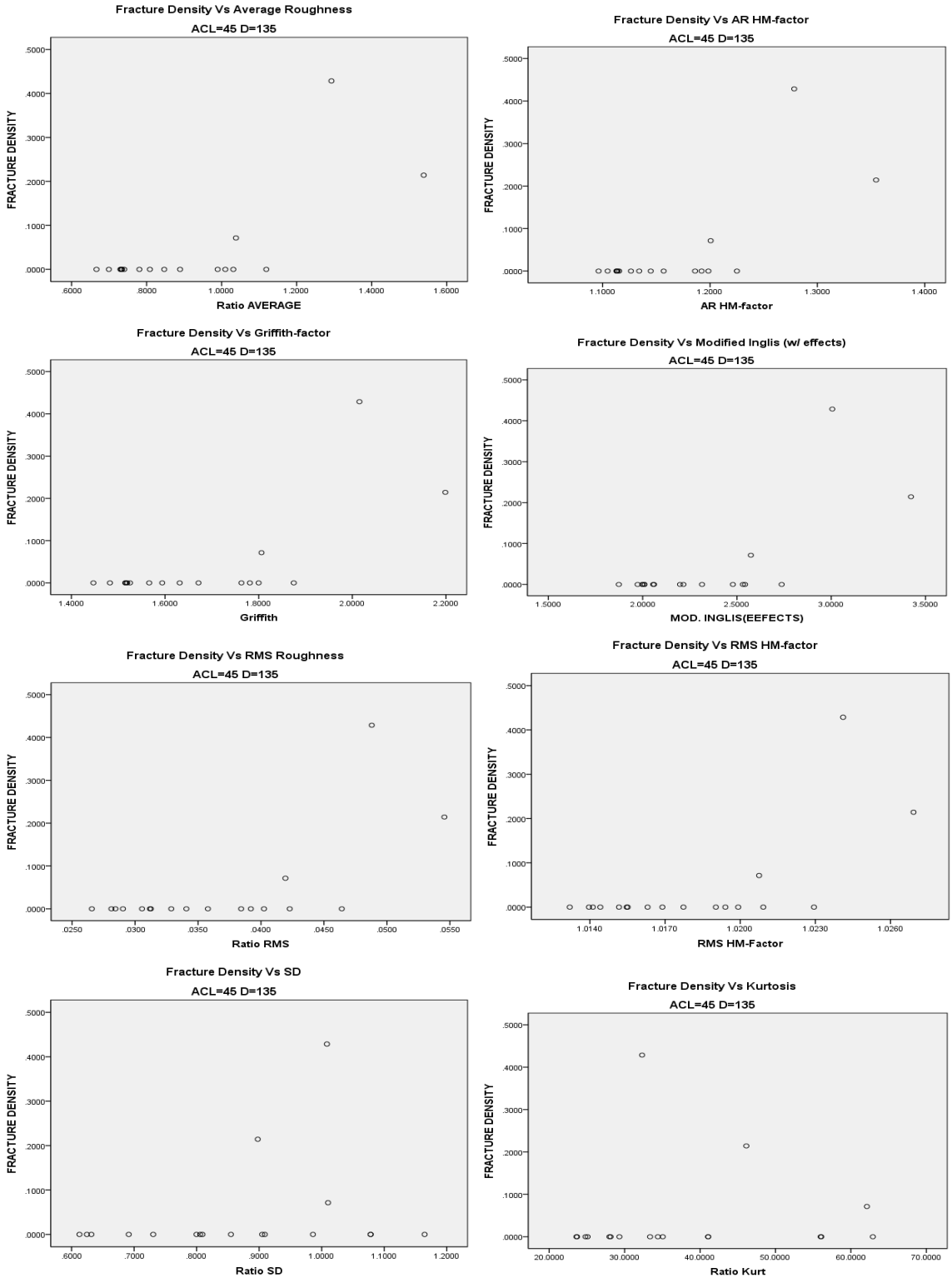

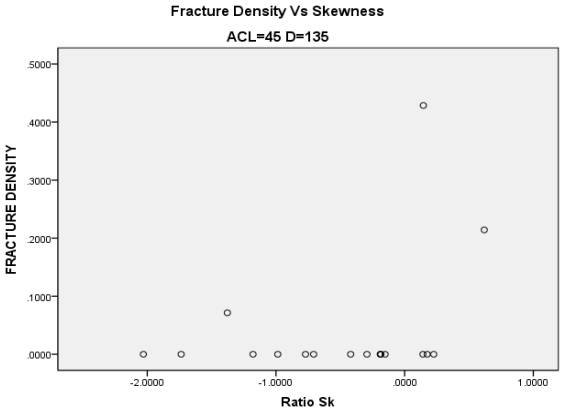
Fracture Density Vs Skewness
ACL=45 D=135
FRACTURE DENSITY
.5000
.4000
.3000
.2000
.1000
.0000
-2.0000
-1.0000
.0000
1.0000
Ratio Sk

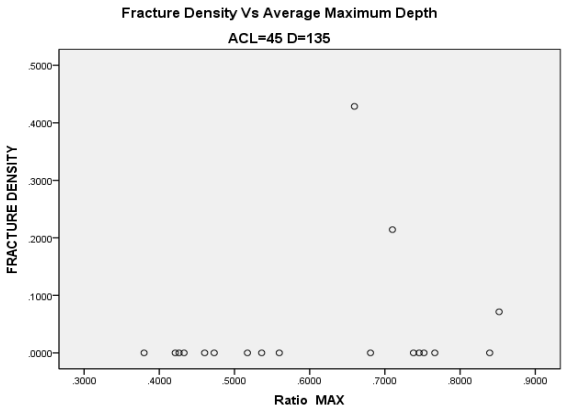
Fracture Density Vs Average Maximum Depth
ACL=45 D=135
FRACTURE DENSITY
.5000
.4000
.3000
.2000
.1000
.0000
.3000
.4000
.5000
.6000
.7000
.8000
.9000
Ratio MAX

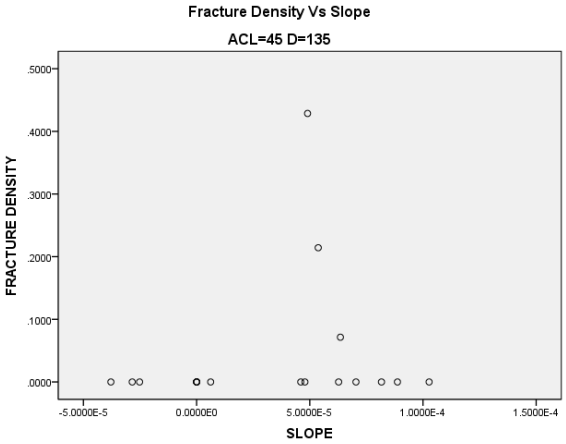
Fracture Density Vs Slope
ACL=45 D=135
FRACTURE DENSITY
.5000
.4000
.3000
.2000
.1000
.0000
-5.0000E-5
0.0000E0
5.0000E-5
1.0000E-4
1.5000E-4
SLOPE

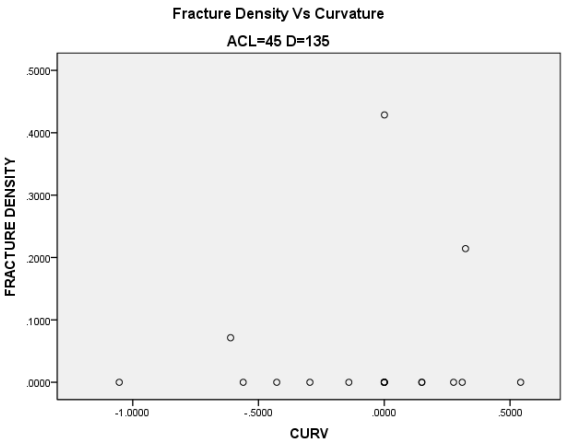
Fracture Density Vs Curvature
ACL=45 D=135
FRACTURE DENSITY
.5000
.4000
.3000
.2000
.1000
.0000
-1.0000
-.5000
.0000
.5000
CURV

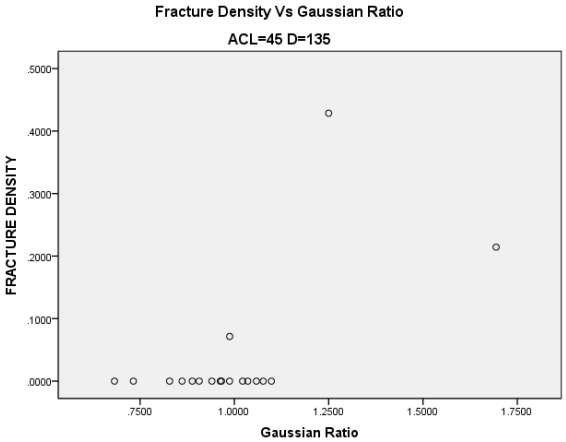
Fracture Density Vs Gaussian Ratio
ACL=45 D=135
FRACTURE DENSITY
.5000
.4000
.3000
.2000
.1000
.0000
.7500
1.0000
1.2500
1.5000
1.7500
Gaussian Ratio

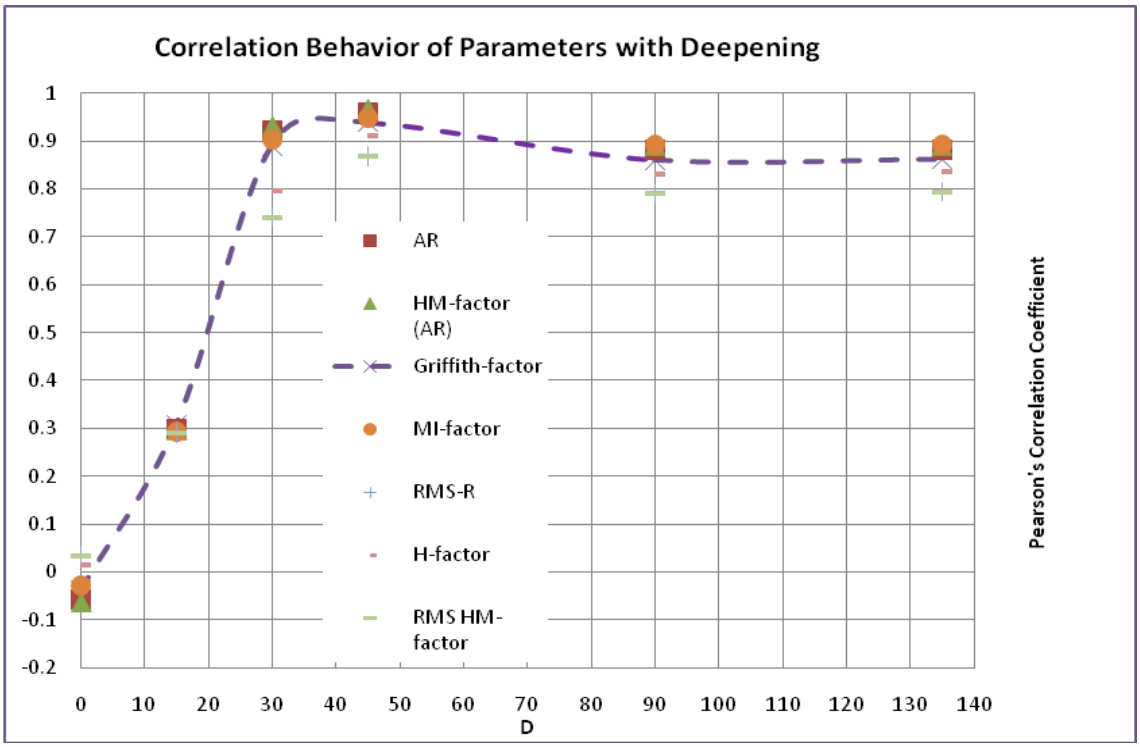

Fig. 5.7 Behavior of Correlation of Fracture Probability (density) with highly correlated Statistical Parameters and Factors for ACL=45

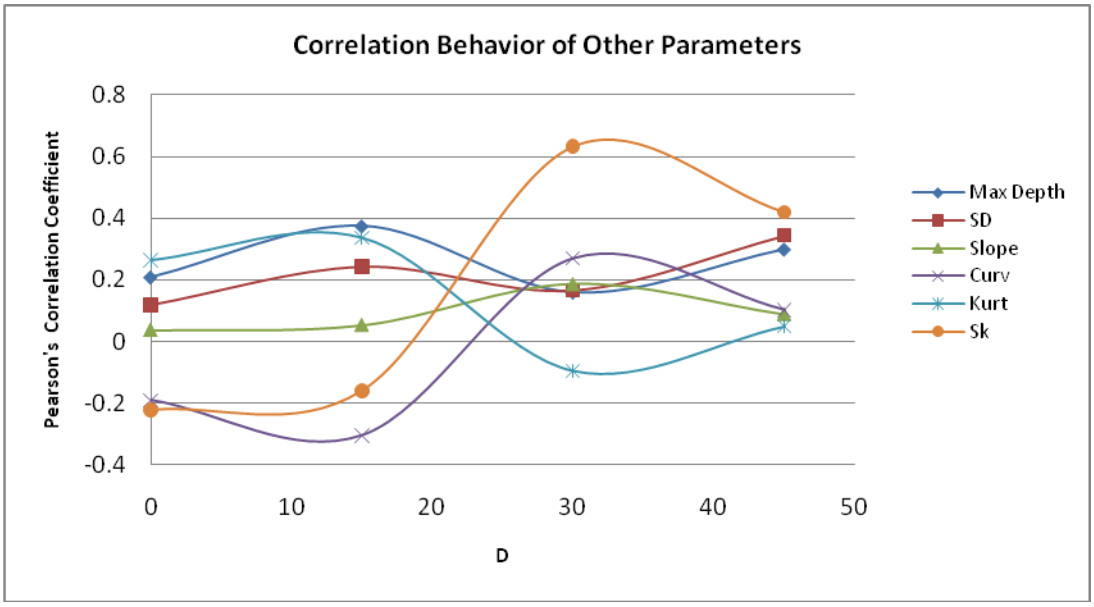

Fig. 5.8 Behavior of Correlation of Fracture Probability (density) with other, low correlated, parameters for ACL=45

5.2 Discussion

It is observed from the scatter plots of the sets of figures 5.1 thru 5.6, that a safety envelopes starts to appear at D=30, for some parameters. As a first approximation, this envelop can be thought of a straight positive-slope line, above which the probability of fracture vanishes. This envelop is very important for designing purposes. The parameters for which this is true are Average Roughness, Root Mean Squared Roughness, Griffith factor, Modified Inglis factor, and RMS-HM factor. Similar Trends are shown for the Skewness and the Standard Deviation. Note that, if the data points at which $\mathcal{H}$ is zero where removed some of the trends shown in those scatter plots would be almost perfectly linearly correlated, as it will be further discussed.

Now let us consider figures 5.7 and 5.8 (ACL=45). In them, Pearson's correlation coefficient has been plotted versus all the parameters studied. Now the first observable is the low-to-zero sensitivity of the fracture location probability at low D values (i.e. $D \lesssim 20$). This means that prediction of failure probability is rather difficult using the aforementioned statistical parameters or factors. This is due to the fact the introduced roughness (in both type and amount) is not sufficient to compete with other factors like internal flaws, impurities, and undesired scratches on the samples. However, it was noticed that roughness introduced does confine failure location probability within the ablated area. In this case, a more micro-scale research must be carried out which is beyond the scope of the present study.

Additionally, as degradation progresses sensitivity of fracture location probability on some parameters gradually increases. More specifically stated, as the accumulation of

vast numbers of small, random assaults increases, fracture location becomes more and more predictable by Average Roughness, RMS Roughness, Griffith Factor, Modified Inglis Factor, RMS H factor, and RMS HM factor. Conclusively, fracture location probability becomes more and more dependent primarily on Average Roughness, Root Mean Squared Roughness, and parameters derived from them. Likewise, from figure 5.8, it can be observed that, dependence of $\mathcal{H}/\mathcal{N}$ on other parameters like Kurtosis, Maximum Depth, Slope and Curvature are rather weak, as deepening increases, for $0 \leq D \leq 135$. The fact that Maximum Pit Depth shows a quite low correlation infers that local isolated deep valleys do not influence Fracture Probability in a significant way.

Now, let us consider the region $0 \leq D \leq 30$, in figure 5.7. Firstly, it represents the transitional region between insensitivity to sensitivity of fracture location probability on the well correlated parameters. Also, it can be noticed that the change is rapid and positive, meaning that small increases in ablation increase significantly the degree of correlation. Conclusively, there is a Transitional Region below which the probability of fracture cannot be predicted by the statistical parameters studied, and above which predictability is very high.

Let us consider now the plateau shown in figure 5.7. As degradation progresses even further ($D>45$), Pearson's correlation Coefficient appears to find an asymptotic limit around the value 0.9, which is significant at the 0.01 level (for a 2-tailed test). This asymptotic limit falls very nicely into the Correlation of the Griffith Criterion Parameter (dotted line in figure 5.7) which agrees with Fracture Mechanics results for brittle materials. As a matter of fact, this is very close the best correlation possible (see section

4.6). As it was discussed, the presence of locations at which H vanishes decreases the highest Pearson's coefficient value of unity. For example, for the cases D=90 and D=135, the highest R obtainable is 0.798. So normalizing the values obtained to this maximum R possible, the actual Pearson's coefficient asymptote value is located around 0.9. For a single notch, this limit would have been unity (1), however because there are multi-site pits, there appears to be some loss of brittleness and gain of ductility. This can easily be visualized by considering an initial stiff wooden beam that shows little to no ductility; then by grooving several notches on it, bending becomes easier and the beam appears to have lost some of its stiffness.

It can also be seen that the *proposed approximation formula* in equation (4.15):

$$k_t = \left[1 + 2\frac{AR}{ACL} \right],$$

Correlates very well with $\mathcal{H}/\mathcal{N}$. Recall that this equation comes from *a novel proposed modification* to the Inglis' formula to the problem of a notch that is not elliptical except at the tip. This could be a significant result, since it is based on an equation used for regular notches. There is a high probability, according to this result, that an analytical solution will involve a polynomial function of pit depth. Another hint that supports this suspicion is obtained from the fact that there was found strong correlation to the parameter obtained from equation

$$\frac{Stress_G(t)}{Stress_G(0)} = \left(1 + \frac{kt}{(Roughness(0))^2} \right)^{-\frac{1}{4}}$$

Proposed by Hinderliter et al [16].

5.3 Summary

1. The first observation is that, for an initial Half Gaussian surface, $\mathcal{H}/\mathcal{N}$ is insensitive to all parameters considered. This means that prediction of failure probability is rather difficult using the aforementioned statistical parameters or factors. This is due to the fact the introduced roughness (in both type and amount) is not sufficient to compete with other factors like internal flaws, impurities, and undesired scratches on the samples. However, it was noticed that roughness introduced does confine failure location probability within the ablated area. In this case, a more micro-scale research must be carried out which is beyond the scope of the present study.
2. The second observation is that as degradation progresses fracture location probability becomes more and more dependent primarily on Average Roughness, Root Mean Squared Roughness, and parameters derived from them. Likewise dependence of $\mathcal{H}/\mathcal{N}$ on other parameters like Kurtosis, Maximum Depth, Slope and Curvature are rather weak, as deepening increases, for $0 \leq D \leq 135$. The fact that Maximum Pit Depth shows a quite low correlation infers that local isolated deep valleys do not influence Fracture Probability in a significant way.
3. There is a transitional region, $D \lesssim 20$, below which the probability of fracture cannot be correlated to any of the statistical parameters studied, and above which there is a rather strong correlation.
4. Additionally, as degradation progresses even further ($D > 45$), Pearson's correlation Coefficient finds a normalized asymptotic limit of around 0.9). This asymptotic limit agrees very nicely with Fracture Mechanics results for brittle materials.

5. It can also be seen that the proposed approximation formula in equation (4.15) correlates very well with the Fracture Density. This could be a significant result, since it is based on an equation used for regular notches. There is a high probability, according to this result, that an analytical solution will involve a polynomial function of pit depth.

5.4 Future Work

As part of the continuation of this study, as Ph. D. research, future work has been started in at least some of the following aspects:

1. Multi-site damage analysis on poly-methyl-methacrylate plates and beams using static loading. The idea is shown in figure 5.9, and it consists on studying laminates of materials with different geometrical discontinuities. As layers deepens the diameters of the circle-shaped and/or axes of the elliptical-shape figures will decrease. So a series of superposition will be developed for each laminate. Then, LEFM approach for each laminate could be used to model the entire system, noticing that these laminates can be thought of as being under tensile stress.
2. Study of thermal effects on the mechanical behavior of PMMA beams with random rough surfaces and compare that behavior with data similar to that shown in figure 2.12b. As temperature increases, brittleness decreases and the effects that multi-site pit roughness is expected to show some interesting results. There might be a critical ductility at which certain roughness.

3. Also, work is being oriented towards a more profound statistical analysis that includes: Partial Correlation, Neural Networks, Weight Estimation, etc. The goal is to develop a more rigorous relationship that will predict failure at early stage of surface degradation.
4. Analysis of stress and strain to fracture of PMMA beams with Random rough surfaces.
5. Fractography analysis of fractured randomly rough PMMA beams under bending.

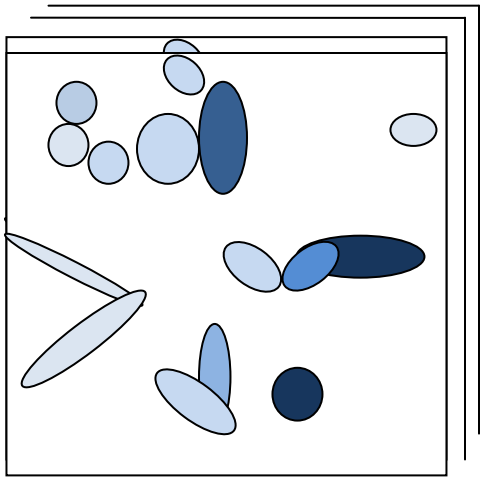

Fig. 5.11: Multi-site damage on several layers of laminates.

Literature Cited

1. Dowling, Norman E., *Mechanical Behavior of Materials: Engineering Methods for Deformation, Fracture and Fatigue*. Third Edition. Page 18.

2. Zobeck, Ted M., *Tillage and rainfall effects on random roughness: A review*. C.A. Onstad. U.S. Department of Agriculture, Agricultural Research Service, P.O. Box 909, Big Spring, TX 79720 U.S.A.

3. Sahoo, Prasanta, *Engineer Tribology*. Prentice-hall of India, New Delhi, India, 2005, page 6.

4. Arismendi, Jorge Alberto et Al, *Machined versus Rough Surface Implants: A Clinical Study*. Revista Facultad de Odontología Universidad de Antioquia, jun2010, Vol. 21 Issue 2, p159-169

5. Prats, Lorenzo M. and Roberson, Mark, *Preventing Fractures in Implant Supported Removable Dentures*, by. Articles of Dentistry Today. December 2010.

6. Ergincan, O. et al., *Influence of Random roughness on cantilever curvature sensitivity*, Applied Physics Letters 96 041912 (2010)

7. Ergincan, O. et al., *Influence of random roughness on cantilever resonance frequency*. Physical Review B 82, 155438 (2010).

8. Jorg Weissmuller et al., *Cantilever Bending with rough surfaces*. Physical Review Letters, PRL 101,146102 (2008).

9. Martin, Jonathan W., Ryntz, Rose A., and Dickie, Ray A., *Service Life Prediction*, Edited by. Federation of Societies for Coatings Technology. 2005

10. Tada, Hiroshi, Paris, Paul C., and Irwin, George R., *The Stress Analysis of Cracks Handbook*, by. Third Edition. ASME, 2000.

11. Bergstrom, Harald, *Limit theorem of Convolution*. Almquist Och Wicksell. Stockholm, and Willey, New York. 1963.

12. Nayak, P. Ranganath, *Random Process Model of Rough Surfaces*. Journal of Lubrication. ASME, 1971.

13. Roark, Raymond J., *Formulas for Stress and Strain*. Fourth Edition. McGraw-Hill Company. 1965

14. Saint-Venant, A. J. C. B., *Mémoire sur la torsion des prismes, Mémoires présentés par divers savants a l'Académie des Sciences*, 1855.14, pp. 233-560

15. Pearson, K. , *Royal Society Proceedings*, 58, 1895, 241.

16. Hinderliter, Brian, and Croll, Stuart, *Predicting Coating Failure using the Central Limit Theorem and Physical Modeling*, Journal of Material Science, 2008, pages 6630-6641.

17. Inglis, C.E., *Stresses in a Plate Due to the Presence of Cracks and Sharp Corners* by. Transactions of the Institute of Naval Architects, Vol 55, 1913, pp. 219-241.

18. Anderson, T.L. *Fracture Mechanics, Fundamentals and Applications*. CRC Press, Inc. 1991.

19. Callister, William D., Jr., and Rethwisch, David G., *Material Science and Engineering, an Introduction*, Eighth Edition.Wiley, 2010.

20. www.mathworks.com

21. Williamson, J.B.P., *The Shape of Surfaces*, CRC Handbook of Lubrication, Volume II, 1983.

22. Williamson, J.B.P., *The Shape of Solid Surfaces, in Surface Mechanics*, Proceedings of the ASME Annual Winter Meeting, Los Angeles, CA, Nov 16-20,1969.

23. ANSI/ASME B46.1-2002 "*Surface Texture* (*Surface Roughness, Waviness and Lay*), American Society of Mechanical Engineers, 2002.

24. ANSI/ASME Y14.36-1996 "*Surface Texture Symbols*",1996

25. ISO 4287:1997 "*Geometrical Product Specifications (GPS) – Surface Texture: Profile method-Terms, definitions and surface texture parameters*.

26. Reed, R.P., Smith, J.H., Christ, B.W., *Economic effects of fracture in the United States. Part1. A synopsis of the September 30,1982 report to NBS by Battelle Columbus Laboratories*. 1983. NTIS, PC A02/MF A01-GPO

27. Duga, J.J., Fisher, W.H., Buxbaum, R.W., Rosenfield, A.R., Buhr, A.R., Honton, E.J., McMillan, S.C., *Economic effects of fracture in the United States. Part2. A report to NBS by Battelle Columbus Laboratories*. 1983. NTIS, PC A16/MF A01-GPO

28. Faria L, rapporteur. *The economic effect of fracture in Europe*. Final report of European Atomic Energy Community study contract no. 320105, 1991

29. Heripre, E., Sun, L., Dubouski, S., Durand, J., *Crack propagation, Wear and Rough Surfaces: Contact Mechanics II*. Solid Mechanics Laboratory, Ecole Polytechnique ParisTech. Paris, 2010.

30. Jiang, H., Bowen, P., Knott, J.F., *Fatigure performance of a cast aluminum alloy Al-7Si-Mg with surface defects*. Journal of Material Science 34 (1999) 719-725

31. Mehdi Tofighi Naeem, Seyed Ali Jazayeri, Nesa Rezamahdi , *Failure Analysis of Gas Turbine Blades.* Proceedings of The 2008 IAJC-IJME International Conference ISBN 978-1-60643-379-9
32. Martin, J.W., Nguyen, T., and Wood, K.A., *Unresolved Issues Related to Predicting the Service Life of Polymeric Materials*. Service Life Prediction chapter 1. Federation of Societies for Coatings Technology, 2005.
33. Al-Mukhtar, A.M., Henkel, S., Biermann, H., Hubner, P., *A finite Element calculation of Stress Intensity Factors of Cruciform and Butt Welded Joints for Some Geometrical Parameters*. Jordan Journal of Mechanical and Industrial Engineering, Volume 3, number 4, December 2009.
34. Garrell, M.G., Shih, A.J., Lara-Curzio, E. , and Scattergood, R.O., Finite *Element Analysis of Stress Concentration in ASTM D 638 Tension Specimens*. Journal of Testing and Evaluation, Volume 31, No 1, by ASTM International, 2003.
35. Haghpanahi, M., and Pirali, H., *Hot Spot Stress Determination for a Tubular T-Joint under Combined Axial and Bending Loading*. International Journal of Engineering Science, Volume 17, No 3-4, 2006, page 21-28.
36. Persson, B.N.J., and Tosatti, E., *The effect of surface roughness on the adhesion of elastic bodies*. Journal of Chemical Physics, Volume 115, number 12. 2001
37. Lin, G., Su, C.H., and Karniadakis, G.E., *Stochastic modeling of random roughness in shock scattering problems: Theory and simulations*. Comput. Methods Appl. Mech. Engrg. 197 (2008) 3420-3434.
38. Devries, K.L., and Nuismer, R.J., Fracture Mechanics of Polymers. American Chemical Society Symposium Series, Chapter 13, pp 277-304. 1985

39. Graystone, J., *Mathematical Implications of Service Life Prediction in the Coatings Industry*. Service Life Prediction chapter 3. Federation of Societies for Coatings Technology, 2005.
40. Gillen, K.T., Celina, M. and Bernstein R., *Methods for predicting Lifetimes and Remaining Lifetimes of Ploymers*. Service Life Prediction chapter 4. Federation of Societies for Coatings Technology, 2005.
41. Rasouli, V., and Harrison, J.P., *Assessment of rock fracture surface roughness using Riemannian statistics of linear profiles*. International Journal of Rocks Mechanics and Mining Sciences, 47 (2010) pp. 940-948.
42. Huang, T.H., Chang, C.S., Chao, C.Y., *Experimental and Mathematical modeling for fracture of rock joint with regular asperities*. Engineering Fracture Mechanics 69 (2002) pp.1977-1996.
43. Al-Ostaz, A., and Jasiuk, I., *Crack Initiation and propagation in materials with randomly distributed holes*. Engineering Fracture Mechanics, Vol. 58 Nos. 5-6 pp.395-420, 1997.
44. Magnusen, P.E., Dubensky, E.M., and Koss, D.A., *The effect of void arrays on void linking during ductile fracture*. Acta Metall. Vol. 36, No. 6, pp. 1503-1509, 1988.

APPENDIX A

Matlab code for Generation of Random Surfaces, Truncating them and Restoring them by Steps

```
% calculate distribution of damage
% surfaces are not really Gaussian early, they start flat and erosion
% removes pieces (down) which leaves a memory until the least removed
% location is down a few pieces deep (CLT)
%%%
%%
% if fullrandom=0, skip ablation generation
fullrandom=0;


format long;
steps=1;

%using 1200 dpi, for a 1/2 x 1/2 inch
N=600;
rL=600;
h=50.;
clx=85;
cly=85;


%Method of convolution based on publication and program of Bergstrom
%(reference in publications)
%generates a fully random surface, after initial surface flatness has
lost
%memory
% rL=12700;
% N=12700;
x = linspace(-rL/2,rL/2,N); y = linspace(-rL/2,rL/2,N);
[X,Y] = meshgrid(x,y);

Z = h.*randn(N,N); % uncorrelated Gaussian random rough surface
distribution
                   % with mean 0 and standard deviation h

% isotropic surface
% Gaussian filter
    F = exp(-((X.^2+Y.^2)/(clx^2/2)));
```

```
% correlation of surface including convolution (faltung), inverse
% Fourier transform and normalizing prefactors
    fBergstrom = 2/sqrt(pi)*rL/N/clx*ifft2(fft2(Z).*fft2(F));

    %way to truncate matrix
    %shift up and down to generate time evolution of surface, only
reaches
    %random after trancation is removed; namely Array1=fBergstrom

    Array3=fBergstrom;

   % WE proceed to truncate the random matrix 9 times in terms of 5
   % units so making increasing the depths of each point on the surface.
   % See sequences produced for further understanding
    fBergstrom12=fBergstrom+5;
    fBergstrom13=fBergstrom+10;
    fBergstrom14=fBergstrom+15;
    fBergstrom15=fBergstrom+20;
    fBergstrom16=fBergstrom+25;
    fBergstrom17=fBergstrom+30;
    fBergstrom18=fBergstrom+35;
    fBergstrom19=fBergstrom+40;
    fBergstrom20=fBergstrom+45;

Array1=(fBergstrom>0).*fBergstrom;
Array12=((fBergstrom12)>0).*fBergstrom12;
Array13=((fBergstrom13)>0).*fBergstrom13;
Array14=((fBergstrom14)>0).*fBergstrom14;
Array15=((fBergstrom15)>0).*fBergstrom15;
Array16=((fBergstrom16)>0).*fBergstrom16;
Array17=((fBergstrom17)>0).*fBergstrom17;
Array18=((fBergstrom18)>0).*fBergstrom18;
Array19=((fBergstrom19)>0).*fBergstrom19;
Array20=((fBergstrom20)>0).*fBergstrom20;

% until here


Array2=255*ones(N,N)-Array1;

% Linecolor none
imwrite(Array1,'your_hdf_file.png')
contourf(Array1,'DisplayName','Array1','linestyle','none');figure(gcf)
axis square
colormap gray
axis off
```

APPENDIX B

Matlab code to transform Surfaces to a PNG picture ready for Laser Ablation

```
% Program to manipulate the arrays that represent random rough surfaces
% This program will produce a PNG picture containing the grayscale
% roughness of the surface.

A=Array2;
B=Array1;
B12=Array12;
B13=Array13;
B14=Array14;
B15=Array15;
B16=Array16;
B17=Array17;
B18=Array18;
B19=Array19;
B20=Array20;

% Lets first normalized to (0,1) and reverse the values, since 0 is
maximum
%dark (darkest) in matlab, but in the original matrix 255 (i.e. 1) is
%maximum ablation
for i=1:600
    for j=1:600
       A1(i,j)=1-A(i,j)/255;
        B1(i,j)=1-B(i,j)/255;
        B121(i,j)=1-B12(i,j)/255;
        B131(i,j)=1-B13(i,j)/255;
        B141(i,j)=1-B14(i,j)/255;
        B151(i,j)=1-B15(i,j)/255;
        B161(i,j)=1-B16(i,j)/255;
        B171(i,j)=1-B17(i,j)/255;
        B181(i,j)=1-B18(i,j)/255;
        B191(i,j)=1-B19(i,j)/255;
        B201(i,j)=1-B20(i,j)/255;

       %let's correct the values according the calibration data of
       %grayscale versus real depth. Values are rescaled between 30
percent
       % and 80 percent black.
       % So, if there is no ablation (1) the value is kept the same, but
if
       % there is some ablation, this value is transformed by the
equation
       % given: new=old*0.5+.2. This comes from the calibration data
       % obtain. See notes for more information. For example, total
       % ablation (zero) is interpreted as .2 (20% dark) since this value
```

```
% is the greatest ablation that can be obtained within the linear
% section of the calibration curve, and very close to the absolute
% maximum ablation.

if A1(i,j)==1
    A2(i,j)=A1(i,j);
else
     A2(i,j)=A1(i,j)*0.5+0.2;
end

  if B1(i,j)==1
    B2(i,j)=B1(i,j);
else
     B2(i,j)=B1(i,j)*0.5+0.2;



  end

 if B121(i,j)==1
    B122(i,j)=B121(i,j);
else
     B122(i,j)=B121(i,j)*0.5+0.2;
 end

if B131(i,j)==1
    B132(i,j)=B131(i,j);
else
     B132(i,j)=B131(i,j)*0.5+0.2;
end

if B141(i,j)==1
    B142(i,j)=B141(i,j);
else
     B142(i,j)=B141(i,j)*0.5+0.2;
end

 if B151(i,j)==1
    B152(i,j)=B151(i,j);
else
     B152(i,j)=B151(i,j)*0.5+0.2;
 end

if B161(i,j)==1
    B162(i,j)=B161(i,j);
else
     B162(i,j)=B161(i,j)*0.5+0.2;
end

if B171(i,j)==1
    B172(i,j)=B171(i,j);
```

```
        else
             B172(i,j)=B171(i,j)*0.5+0.2;
        end

        if B181(i,j)==1
            B182(i,j)=B181(i,j);
        else
             B182(i,j)=B181(i,j)*0.5+0.2;
        end

        if B191(i,j)==1
            B192(i,j)=B191(i,j);
        else
             B192(i,j)=B191(i,j)*0.5+0.2;
        end

        if B201(i,j)==1
            B202(i,j)=B201(i,j);
        else
             B202(i,j)=B201(i,j)*0.5+0.2;
        end

    end

end



% Now we proceed to make the roughness images using the transformed
% matrices
imwrite(B2,'C:\Users\medinahe\Documents\RESEARCH\Material
Mechanics\pattern of random surfaces\roughcorrected_1.png');
imwrite(B122,'C:\Users\medinahe\Documents\RESEARCH\Material
Mechanics\pattern of random surfaces\roughcorrected_2.png');
imwrite(B132,'C:\Users\medinahe\Documents\RESEARCH\Material
Mechanics\pattern of random surfaces\roughcorrected_3.png');
imwrite(B142,'C:\Users\medinahe\Documents\RESEARCH\Material
Mechanics\pattern of random surfaces\roughcorrected_4.png');
imwrite(B152,'C:\Users\medinahe\Documents\RESEARCH\Material
Mechanics\pattern of random surfaces\roughcorrected_5.png');
imwrite(B162,'C:\Users\medinahe\Documents\RESEARCH\Material
Mechanics\pattern of random surfaces\roughcorrected_6.png');
imwrite(B172,'C:\Users\medinahe\Documents\RESEARCH\Material
Mechanics\pattern of random surfaces\roughcorrected_7.png');
imwrite(B182,'C:\Users\medinahe\Documents\RESEARCH\Material
Mechanics\pattern of random surfaces\roughcorrected_8.png');
imwrite(B192,'C:\Users\medinahe\Documents\RESEARCH\Material
Mechanics\pattern of random surfaces\roughcorrected_9.png');
imwrite(B202,'C:\Users\medinahe\Documents\RESEARCH\Material
Mechanics\pattern of random surfaces\roughcorrected_10.png');
```

APPENDIX C

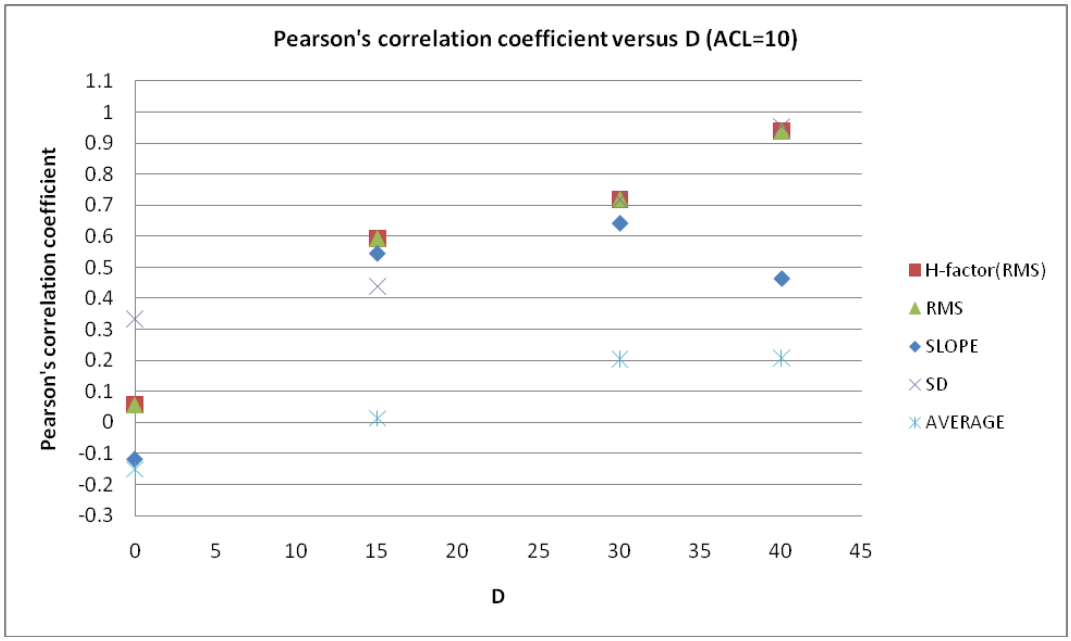

Fig. C.1 Behavior of Correlation of Fracture Probability (density) with some parameters for ACL=10

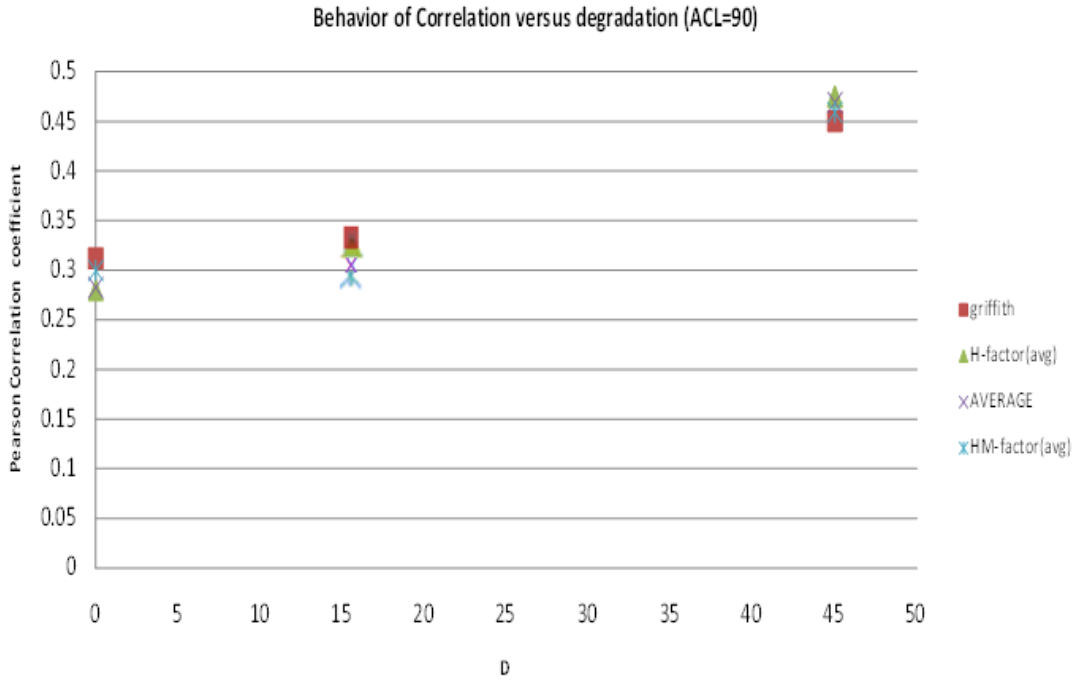

Fig. C.2 Behavior of Correlation of Fracture Probability (density) with some parameters for ACL=90

VITA

Hector E. Medina was born in August 21, 1971 in Cocollar, a southern small town of Sucre State, in the Eastern Coast of Venezuela, South America. During his primary school years, he had to work half day at the public market, in order to buy books and shoes. After graduating from High School, he earned the highest scholarship that the Venezuelan Government offers: THE GRAN MARISCAL DE AYACUCHO Scholarship. Under it, he was sent to the Colorado School of Mines, in Golden Colorado, to learn English and to pursue his Bachelor's Degree in Mechanical Engineering, which He earned in December of 1994 with High Scholastic Honors, Outstanding International Student Achievement, and several other awards. At that time, He was approached by the Mechanical Engineering Department Chair and offered a scholarship to pursue a doctoral degree, which was forced to reject due to personal reasons. After working for several years in several companies in Venezuela and Aruba, and due to his aspiration to teaching, he decided to return to school to pursue graduate studies at the Virginia Commonwealth University, in Richmond, Virginia.